

RBF level-set based fully-nonlinear fluorescence photoacoustic pharmacokinetic tomography

Omprakash Gottam, Naren Naik, Prabodh Kumar Pandey & Sanjay Gambhir

To cite this article: Omprakash Gottam, Naren Naik, Prabodh Kumar Pandey & Sanjay Gambhir (2021) RBF level-set based fully-nonlinear fluorescence photoacoustic pharmacokinetic tomography, Inverse Problems in Science and Engineering, 29:13, 3227-3260, DOI: [10.1080/17415977.2021.1982934](https://doi.org/10.1080/17415977.2021.1982934)

To link to this article: <https://doi.org/10.1080/17415977.2021.1982934>



Published online: 04 Oct 2021.



Submit your article to this journal [↗](#)



Article views: 104



View related articles [↗](#)



View Crossmark data [↗](#)



RBF level-set based fully-nonlinear fluorescence photoacoustic pharmacokinetic tomography

Omprakash Gottam^a, Naren Naik^{a,b}, Prabodh Kumar Pandey^c and Sanjay Gambhir^d

^aDepartment of Electrical Engineering, Indian Institute of Technology Kanpur, India; ^bCenter for Lasers and Photonics, Indian Institute of Technology Kanpur, Kanpur, India; ^cDepartment of Physics, Indian Institute of Technology Kanpur, Kanpur, India; ^dDepartment of Nuclear Medicine, Sanjay Gandhi Postgraduate Institute of Medical Sciences, Lucknow, India

ABSTRACT

Pharmacokinetic fluorescence optical tomography (PK-FOT) and dynamic contrast enhancement (DCE) based multispectral photoacoustic tomography (DCE-MSOT) are non-ionizing alternatives to nuclear medicine and radiological modalities such as DCE-PET/CT/MRI for spatially-resolved quantitative imaging of PK parameters and fluorophore-concentrations. The present work introduces for the first time in literature, a fluorescence photoacoustic tomography (FPAT) based fully-nonlinear PK-FPAT reconstruction framework; in a 2-compartment PK-model and optical-fluorescence modelled frequency domain photoacoustic equation setting. From boundary pressure measurements, we solve the dynamic FPAT (compartment-concentration) state and (PK) parameter estimation problem with two shape-based RBF level-set reconstruction schemes in regularized trust region settings; a Jacobian-based Gauss–Newton filter and our newly proposed gradient-based gradient filter. The reconstruction algorithms are validated in two dimensional settings with synthetic cancer mimicking phantoms. Our PK-FPAT algorithms lead to more stable and superior reconstructions (observed in reconstructed normalized mean square errors having lesser-variation-between and reduced-values-across data-noise levels, respectively) than those obtained by PK-FOT for similar test cases, while, with respect to current DCE-MSOT schemes, incorporating more complete forward models including optical fluorescence and coupled-ODE compartment models with no simplifying assumptions (within the accuracy of the models considered) on the fluence, and reconstructing actual (rather than scaled) PK-parameters, in a fully-nonlinear framework.

ARTICLE HISTORY

Received 26 March 2021

Accepted 13 September 2021

KEYWORDS

Pharmacokinetic tomography; fluorescence photoacoustic tomography; level-set based reconstructions; regularized Gauss–Newton filter; regularized gradient filter; early cancer detection; functional imaging

MATHS

92C45; 92C55; 94A08

1. Introduction

Pharmacokinetic rates of contrast agents provide quantitative physiological information for analysing the vascular permeability characteristics of blood vessels in the tissue, in early cancer detection and drug metabolism studies. Nuclear medicine and radiological imaging modalities such as PET, MRI, or CT are used for pharmacokinetic (PK) imaging

CONTACT Naren Naik ✉ nnaik@iitk.ac.in Department of Electrical Engineering, Indian Institute of Technology, Kanpur, India

based upon the dynamic contrast enhancement (DCE) of the injected contrast agents[1–8]. Non-ionizing alternatives to these include those based upon fluorescence optical tomography(FOT) in single modality [9–13] or hybrid FOT-X-ray-CT schemes[14–16], or multi-spectral optoacoustic tomography(MSOT) [17–21]. First preliminary PK-reconstructions using the upcoming modality of fluorescence photoacoustic tomography(FPAT) have been recently shown by us in a Gauss–Newton filter framework [22].

DCE-MSOT seeks to overcome the issues of poor-temporal resolution or spatio-temporal resolution-tradeoff in CT/PET/MRI-based DCE, or the high cost of CT/MRI-DCE systems that have good spatial and temporal resolution. Current DCE-MSOT schemes [17,21] use region-of-interest compartment PK-models and constraints regarding spatial/temporal properties of the fluence distributions, on the photoacoustic signals (instead of the underlying concentrations) to obtain approximate scaled estimates of PK-parameters via pixel-wise linear/nonlinear-model based regression, from first stage reconstructions of the photoacoustic signal. We recall that the photoacoustic signal refers to the absorbed optical energy density source obtained from inversion of the measured pressure data. They differ from previous MSOT-based approaches such as in the qualitative [20] or semi-quantitative [18] approaches, in that they give a quantitative DCE-MSOT framework that does not need the photoabsorber-concentrations in each pixel as inputs, in addition to dispensing with the need for optical fluence correction via suitable approximations on the fluence distribution, such as the its spatial constancy in background components and time-invariance.

However, primary conceptual limiting assumptions in [17] about the fluence only changing in pixels where the contrast agent accumulates with the endogeneous fluence staying constant, and, assuming that the contrast agent concentration in the plasma is known as function of time; in addition to the fluorescence propagation not being considered in the modelling process. In our present work, we propose for the first time in literature, a fully-nonlinear dynamic FPAT reconstruction framework from boundary pressure measurements for quantitative PK parameters and fluorophore-concentrations, using an optical-fluorescence modelled frequency-domain photoacoustic-equation and coupled 2-PK-compartment-model. We thus do not need any assumptions on the fluence or on the concentration of the fluorophore in the plasma(other than the use of a coupled-compartment model).

PK-FOT works such as in [9,11–13] utilize physiological/functional compartment models to obtain tomographic reconstructions of PK-rates from measured excitances; these rates are used to determine metabolic behaviour in the region of interest. Photoacoustic tomography has been proposed as an augmentation to stabilize the FOT reconstructions by reconstructing the optical parameters from photoacoustically generated pressure data; thus yielding fluorescence photoacoustic tomography (FPAT) [23,24]. Also, as is well known, quantitative photoacoustic tomography, (resp. it's fluorescence counterpart, FPAT) while retaining good optical contrast properties, enables better resolution quantitative optical-parameter information to be retrieved from greater depth [25] than is possible using only diffuse optical tomography (resp., FOT).

The emerging of fluorescent markers having high quantum efficiencies and low toxicity[26] necessitate the taking of fluorescence propagation into account in the photoacoustic process, yielding FPAT formulations rather than the quantitative photoacoustic tomography [23]. Fluorescence photoacoustic tomography (FPAT) has been proposed to

recover the absorption coefficient of the fluorophore from measured pressure data, in a static setting [23,24,27–29]. In [24,29], a two-step method is assumed, where the absorbed optical energy density is reconstructed from the pressure signal followed by recovery of the absorption coefficient from the absorbed optical energy density. The use of one-step schemes in FPAT recovering the fluorophore absorption coefficient directly from the pressure signal using Jacobian or gradient information in a one-step framework, have been proposed recently in [23,27] and [28] corresponding to optical propagation being modelled in the diffuse approximation and the full radiative transfer equation, respectively. The motivation of using gradient-based schemes stems from the computational complexity of the adjoint problem in the measurement Jacobian-based methods being $\mathcal{O}(N)$ (N being the number of nodes in the domain) as compared to that for the adjoint problem in costfunction-gradient computation being $\mathcal{O}(1)$) [28]. On the other hand, the number of iterations consumed by Jacobian-based reconstruction schemes such as the Gauss–Newton method are usually much less than that for the gradient-based BFGS-type schemes owing to second-order information used in the Gauss–Newton method as against the first-order information-based gradient schemes.

Shape-based reconstructions in tomographic imaging reduce the search space dimensions and improve computational feasibility in large scale and dynamic problems, in addition to potentially reducing clutter in limited-data reconstructions [30–33]. A 2D Gauss–Newton filter-based PK-FOT reconstruction scheme has been formulated in a radial basis function (RBF) based level-set framework [11]; the scheme uses the nonlinear optical fluorescence-based measurement equation and a coupled-ODE 2-compartment PK-model.

The dynamic pharmacokinetic problem can be solved using statistical methods like Kalman filter [9,10] or deterministic methods like Gauss–Newton filter [31,34]. We further propose a gradient filter framework in our present work, to reduce the computational complexity involved in the Jacobian-based Gauss–Newton filter method. The present work proposes fully nonlinear Gauss–Newton filter (GNF) and gradient filter (GF) reconstruction schemes in a regularized trust-region framework for one-step PK-FPAT from photoacoustic pressure data, in an RBF-based level-set setting for a 2-compartment coupled-ODE PK-model. A Hermite interpolation-based noncompact-RBF representation is used for the level-set description of the boundary of the inhomogeneity/pathology [31,32].

We mention with respect to DCE-MSOT formulations such as in [17,21], that, in our complete-model-based PK-tomographic reconstruction framework, the coupled-ODE 2-compartment model-based dynamical state-equations used are directly in terms of the concentrations and not approximations w.r.t an intermediate photoacoustic signal. No assumptions are made on the fluence or underlying compartment-wise concentrations in the course of the formulation; the one-step reconstruction scheme takes into account the full nonlinear relationship between the pressure data and the underlying concentrations/absorption-coefficients, without needing to reconstruct the intermediate photoacoustic signal (the absorbed optical energy density). Moreover, the PK parameters reconstructed in our work are the actual parameters and not their scaled approximations.

The algorithmic methodology sets up a state-space model governing the tomographic process using a 2-compartment model-based coupled-ODE state-equation and fluorescent photoacoustic measurement equation. The (time-varying) states are designated as

the spatially-resolved compartment-wise concentrations, and the (temporally constant) parameters are the spatially resolved pharmacokinetic parameters and volume fractions. We then solve the corresponding state and parameter estimation problem with boundary photoacoustic pressure measurements using regularized GNF and GF schemes in a trust-region framework. For the GNF, we derive the requisite Jacobians relating the change in the boundary measurements to the change in the exogeneous fluorophore's pharmacokinetic rates, concentrations, volume fractions and the shape parameters. For the GF, the gradients relating the change in cost function to the above mentioned parameters are derived.

We have modeled the photoacoustic process by the frequency domain (Helmholtz) photoacoustic equation, and the corresponding optical propagation through tissue by a set of coupled diffusion-approximation equations at the excitation and emission wavelengths.

The validation of the proposed algorithm is carried out on synthetic test cases of cancer mimicking phantoms of invasive ductal carcinoma (IDC) and adenocarcinoma (AC) types, for various noise levels in the data. To the best of our knowledge, this is the first PK-FPAT formulation and study in literature.

The present work goes beyond the recent preliminary results presented by us [22] in that:

- (a) We have proposed and numerically validated a regularized gradient filter (GF) reconstruction scheme in addition to the earlier Gauss–Newton filter (GNF) scheme.
- (b) The detailed formulation and derivation of the GNF Jacobians and GF gradient and corresponding schemes have been given in the present manuscript, and, detailed numerical studies have now been included for tumour-mimicking phantoms of two different kinds of cancer (invasive ductal carcinoma and adenocarcinoma) for various noise levels in the data and importantly the results have been well quantified by error-metrics.

This paper follows our earlier paper on pharmacokinetic fluorescence optical tomography (PK-FOT) [11], and conceptually differs/builds from it in that: (a) We have now obtained reconstruction schemes for the PK-FPAT problem; the earlier paper was about PK-FOT, (b) we have proposed a regularized gradient filter reconstruction scheme and apply it to PK-FPAT, in addition to the trust-region-based Gauss–Newton filter scheme used in our previous work. (c) We have used non-compactly supported Hermite interpolation-based RBFs in the present work as against the compactly supported RBFs used in the previous work

In Section 2, we describe the fluorescence-based photoacoustic process model and compartment modelling of the fluorophore pharmacokinetics, in addition to stating the problem of PK-FPAT. In Section 3, we present the PK 2-compartment model-based state–space framework, in a non-compact RBF-based level-set representation of the states and parameters. Section 4 derives the Jacobians and gradients needed for the GNF and GF schemes, respectively, with Section 5 presenting the reconstruction schemes employed. Numerical validation of the algorithms and discussion of results are contained in Section 5. Summary and conclusions are given in Section 6. Appendix 1 contains the requisite expressions of adjoint field calculations needed in gradient calculations for the GF. Appendix 2 contains the definitions of the error measures. List of acronyms are given in Appendix 3.

2. Background: tomographic process and problem statement

2.1. Process overview

Fluorescent contrast agents have the potential to aid cancer detection by binding to the blood plasma, forming a macromolecule and leaking into the cancerous tissue [35]. After mixing a drug with fluorophore marker and its injection into the body (using IV bolus), laser light is irradiated into the region of interest at the excitation wavelength of the marker and that, along with emitted fluorescent light create a heat source in the pathological domain (photoacoustic heating), leading to a pressure wave propagating in the medium. The compartmental concentrations and PK-rates of the injected fluorophores can be tomographically monitored in the body with FPAT by using measurements of pressure waves (originating from the fluorophore and haemoglobin) generated due to photoacoustic heating of the region of interest.

Pressure-wave time-series are recorded at each measurement time (the time-span of each such pressure time-series being very small compared to the measurement time spacing). The pressure time-series at each measurement time is Fourier transformed into corresponding frequency domain pressure data (as shown in the numerical studies section); in our work, the acoustic wave propagation model considered is the frequency-domain Helmholtz equation. Fluorescent light propagation in the medium can be described using coupled excitation-emission propagation equations in the diffusion approximation for radiative transfer.

Reconstruction schemes are proposed by means of obtaining the best possible optical parameters that fit the measured data, in our work, via the minimization of a nonlinear least squares data-residual-functional, as described in the sequel.

2.2. Models for the FPAT process

When a short-pulsed laser source (fulfilling the thermal confinement conditions) illuminates the tissue, energy is absorbed by the fluorophores and chromophores. The absorbed energy causes thermoelastic expansion in the tissue, which leads to a pressure wave generation. The propagation of the pressure wave in an homogenous acoustic medium with the excitation pulse satisfying the thermal and stress confinement conditions is described in the frequency domain by the photoacoustic equation [36]:

$$(\nabla^2 + k^2)p(\vec{r}, k) = ik \frac{v\beta}{c^p} h(\vec{r}) \quad \text{in } \Omega \quad (1)$$

with the Sommerfeld radiation condition given by [37,38]

$$\vec{n} \cdot \nabla p(\vec{r}, k) + ikp(\vec{r}, k) = 0 \quad \text{on } \partial\Omega \quad (2)$$

where v is the speed of acoustic wave in the medium, β is the thermal expansion coefficient, c^p is the specific heat, $k = \omega_p/v$ is the wave number at angular frequency ω_p , and $h(\vec{r})$ is the absorbed optical energy density, given by:

$$h(\vec{r}) = (\mu_{axf}(\vec{r}) + \mu_{axi}(\vec{r}))\Phi_x(\vec{r}) + (\mu_{amf}(\vec{r}) + \mu_{ami}(\vec{r}))\Phi_m(\vec{r}). \quad (3)$$

where (' x/m ' stands for either ' x ' (excitation) or ' m ' (emission)) Φ_x (J/mm²) is the excitation photon density, Φ_m (J/mm²) is the emission photon density, $\mu_{a(x/m)i}$ and $\mu_{a(x/m)f}$

being the absorption coefficients due to intrinsic chromophores and extrinsic fluorophores, respectively. In the diffusion approximation, the absorption coefficients and the photon density are related through the coupled diffusion equations [39]:

$$\begin{aligned} -\nabla \cdot (D_x \nabla \Phi_x) + k_x \Phi_x &= S_x \\ &\text{in } \Omega \\ -\nabla \cdot (D_m \nabla \Phi_m) + k_m \Phi_m &= \eta \Phi_x \end{aligned} \quad (4)$$

subject to the Robin boundary conditions

$$\begin{aligned} \vec{n} \cdot (D_x \nabla \Phi_x) + b_x \Phi_x &= 0 \\ &\text{on } \partial\Omega \\ \vec{n} \cdot (D_m \nabla \Phi_m) + b_m \Phi_m &= 0 \end{aligned} \quad (5)$$

$$D_{x/m} = \frac{1}{3(\mu_{a(x/m)i} + \mu_{a(x/m)f} + \mu'_{s(x/m)})}, \eta = \phi_q \mu_{axf}, b_{x/m} = \frac{1 - R_{(x/m)}}{2(1 + R_{(x/m)})},$$

$$k_{x/m} = \mu_{a(x/m)i} + \mu_{a(x/m)f}$$

S_x (J/mm^2) is the laser excitation source, $D_{x/m}$ is the diffusion coefficient at excitation/emission wavelength, $k_{x/m}$ is a decay coefficient, $\mu'_{s(x/m)}$ being the respective reduced scattering coefficient, (all in mm^{-1}) at the two wavelengths, η is the quantum yield (as defined in [24,40]) and ϕ_q being the fluorescence quantum efficiency [24,29,40–42], $b_{x/m}$ are Robin boundary coefficients, $R_{x/m}$ are the Fresnel reflection coefficients.

2.3. Compartmental pharmacokinetic models

A two compartment model is used [9,11,43], to describe the fluorophore exchange in the region of interest, which is divided into a plasma compartment and an extracellular and extravascular space (EES) compartment as shown in Figure 1. The concentration of the fluorophore is linked to the absorption coefficient of the fluorophore by the following relation [9]:

$$\mu_{a(x/m)f}(\vec{r}, t) = \ln 10 \cdot \varepsilon_{(x/m)} \cdot C(\vec{r}, t) \quad (6)$$

where $\varepsilon_{x/m}$ is the fluorophore molar extinction coefficient, $C(\vec{r}, t)$ is the total fluorophore concentration in the tissue.

We note from Equation (6) that we can write $\mu_{amf} \equiv \varepsilon_s \mu_{axf}$, where $\varepsilon_s \equiv \varepsilon_m / \varepsilon_x$.

Now, $C(\vec{r}, t)$ is given by [9]

$$C(\vec{r}, t) = v_p(\vec{r}) C_p(\vec{r}, t) + v_e(\vec{r}) C_e(\vec{r}, t) \quad (7)$$

Here, C_p (μM) and C_e (μM) (respectively, v_p and v_e) denote the concentration (respectively, volume fraction) of the fluorophore in the plasma and EES compartment, respectively. Volume fraction of a particular compartment is defined as the ratio of volume of distribution in that compartment to the total volume of distribution ($V = V_e + V_p$).

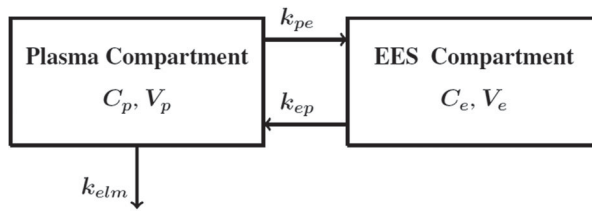


Figure 1. Block diagram of two compartment model.

The dynamic concentration of optical parameters μ_{axf} and μ_{amf} is assumed to vary as per the compartment-modelled coupled ODE-system [9,11]

$$\dot{\mathbf{C}}(\vec{r}, t) = \mathbf{K}(k_{pe}(\vec{r}), k_{ep}(\vec{r}), k_{elm}(\vec{r}))\mathbf{C}(\vec{r}, t) \quad (8)$$

where \vec{r} denotes spatial coordinates and $\mathbf{C}(\vec{r}, t) = \begin{bmatrix} C_e(\vec{r}, t) \\ C_p(\vec{r}, t) \end{bmatrix}$; $\mathbf{K}(k_{pe}(\vec{r}), k_{ep}(\vec{r}), k_{elm}(\vec{r})) = \begin{bmatrix} -k_{ep}(\vec{r}) & k_{pe}(\vec{r}) \\ k_{ep}(\vec{r}) & -(k_{pe}(\vec{r}) + k_{elm}(\vec{r})) \end{bmatrix}$

Here, k_{pe} (s^{-1}) denotes the transfer rate of fluorophore from plasma to EES compartment, k_{ep} (s^{-1}) denotes the transfer rate of fluorophore from EES to plasma compartment, k_{elm} (s^{-1}) is the rate at which fluorophore is eliminated from region of interest. In the case of invasive ductal carcinoma (IDC), the value of k_{pe} is reported in the range of 0.069 inside the tumour and 0.03 outside the tumour [10], k_{ep} is reported around 0.049 inside the tumour and 0.017 outside the tumour [10]. High pharmacokinetic rates in the tumour region results in high volume fractions; the range of v_e (resp. v_p) being given in [7](resp. [35,43]) as 0.2 to 0.5 (resp. 0.013 to 0.067).

The discrete time state model corresponding to time instants t_j and t_{j+1} (indexed as j and $j+1$, respectively) for (8) is given by [9,44]

$$\mathbf{C}(\vec{r}, j+1) = \mathbf{T}(\tau_{11}(\vec{r}), \tau_{12}(\vec{r}), \tau_{21}(\vec{r}), \tau_{22}(\vec{r}))\mathbf{C}(\vec{r}, j) \quad (9)$$

where

$$\mathbf{T} \equiv e^{\mathbf{K}\Delta t} \equiv \begin{bmatrix} \tau_{11}(\vec{r}) & \tau_{12}(\vec{r}) \\ \tau_{21}(\vec{r}) & \tau_{22}(\vec{r}) \end{bmatrix} \quad (10)$$

and $\Delta t = t_{j+1} - t_j$ is the measurement sampling interval.

2.4. The reconstruction problem

The inverse problem of reconstructing from the pressure data the unknown pharmacokinetic rates (k_{pe} , k_{ep} , k_{elm}), concentrations (C_e and C_p) and volume fractions (v_e and v_p) is proposed with non-compact RBF level-set based GNF and GF schemes. The sensitivities of the measured data as well as the cost-function-gradient with respect to unknown parameters are derived using the frequency domain Helmholtz equation (to model pressure signal propagation) and coupled diffusion equation (to model light propagation) for reconstructing the pharmacokinetic parameters directly from the boundary pressure measurements.

3. RBF level-set based 2-compartment PK state-model

3.1. Shape representation

The contrast in the pharmacokinetic rates [9,11] around the cancerous tissue compared to the healthy tissue is due to leaky vasculature around the cancerous tissue [35,45]. Assuming the rates to be piece-wise constant, they can be represented as [11,31]:

$$k_{\xi}(\vec{r}) = k_{\xi}^i(\vec{r})H_{\epsilon}(s(\vec{r})) + k_{\xi}^o(\vec{r})(1 - H_{\epsilon}(s(\vec{r}))) \quad (11)$$

where $\xi \in \{ep, pe, elm\}$, and $k_{\xi}^i(\vec{r})$ and $k_{\xi}^o(\vec{r})$ are the values inside and outside the tumour region, respectively. H_{ϵ} represents a mollified Heaviside function with transition half-width ϵ [32,46], and $s(\vec{r})$ is a function whose zero level-set represents the boundary of the tumour, and whose value is positive (resp. negative) inside (resp. outside) the tumour region; in our work we use a signed-distance function for s .

In this work $s(\vec{r})$ is represented using RBF via a Hermite interpolation scheme [31,32,47] to fit a few on-curve points (called the centres of the RBF, and denoted by $\mathbf{r}_1^c, \dots, \mathbf{r}_m^c$, m denotes the number of RBF centres used) and the normal unit vectors to the boundary at those points (denoted by $\mathbf{n}_1, \dots, \mathbf{n}_m$ where $\mathbf{n}_i \equiv (\cos\theta_i^c, \sin\theta_i^c)$ for some θ_i^c). The level-set function can be written in the form as [32]

$$s(r) = p_s(r) + \sum_{j=1}^m [c_j \Phi(r - r_j^c) - d_j (D_{\mathbf{n}_j} \Phi)(r - r_j^c)] \quad (12)$$

where $p_s(\cdot)$ is a (typically) low-order polynomial of degree $k-1$, $\Phi(\cdot) \equiv \phi(\|\cdot\|)$, with ϕ in our work being an unbounded and non-compactly supported real valued function on $[0, \infty]$ called the basic function; Φ is chosen a twice continuously differentiable function conditionally positive definite of order k in the appropriate sense, and $D_{\mathbf{n}_j} \psi(r) \equiv \mathbf{n}_j \cdot (\nabla \psi)(r)$ denotes the directional derivative functional w.r.t a unit normal \mathbf{n}_j . The coefficients c and d are RBF coefficients.

In the two-dimensional setting considered in this work, the shape parameters are the RBF-centre coordinates $\{r_j^c \equiv (x_j^c, y_j^c), j = 1, \dots, m\}$ and unit normals represented using the angles $\{\theta_c^j, j = 1, \dots, m\}$, corresponding in the vector notation to $\mathbf{x}^c, \mathbf{y}^c, \boldsymbol{\theta}^c$.

The concentrations C_e and C_p and volume fractions v_e and v_p are spatially dependent on pharmacokinetic rates. Hence their level-set representation is given by [11]:

$$\begin{aligned} C_{(e/p)}(\vec{r}, j) &= C_{(e/p)}^i(j)H_{\epsilon}(s(\vec{r})) + C_{(e/p)}^o(j)(1 - H_{\epsilon}(s(\vec{r}))) \\ v_{(e/p)}(\vec{r}) &= v_{(e/p)}^i(\vec{r})H_{\epsilon}(s(\vec{r})) + v_{(e/p)}^o(\vec{r})(1 - H_{\epsilon}(s(\vec{r}))) \end{aligned} \quad (13)$$

where $C_{(e/p)}^i$ (resp. $v_{(e/p)}^i$) and $C_{(e/p)}^o$ (resp. $v_{(e/p)}^o$) are assumed piecewise constant values of concentration (resp. volume fraction) inside and outside the tumour, respectively. Using the level-set representation of concentrations and volume fractions, the relation between $\mu_{a(x/m)f}$ and C can be written at each time instant, in the form of Equation (11) as:

$$\mu(\vec{r}, j) = \ln 10 \cdot \varepsilon \cdot [(C_e(j)^i v_e^i + C_p(j)^i v_p^i) H_{\epsilon}(s(\vec{r})) + (C_e(j)^o v_e^o + C_p(j)^o v_p^o) (1 - H_{\epsilon}(s(\vec{r})))] \quad (14)$$

where the subscripts on μ have been omitted for ease of notation.

3.2. State equation

We set up the compartment model-based state equation as we have previously derived in [11], and is written as

$$\Theta_{j+1} = A(\Theta_j) \cdot \Theta_j \equiv f_j(\Theta_j) \quad (15)$$

where f denotes the nonlinear state transition function and, matrix $A(\Theta_j)$ is

$$A(\Theta_j) \equiv \begin{bmatrix} T^i & 0 & 0 \\ 0 & T^o & 0 \\ 0 & 0 & I_{3m+10} \end{bmatrix}; \quad T^{i/o} = \begin{bmatrix} \tau_{11}^{i/o}(\mathbf{k}) & \tau_{12}^{i/o}(\mathbf{k}) \\ \tau_{21}^{i/o}(\mathbf{k}) & \tau_{22}^{i/o}(\mathbf{k}) \end{bmatrix} \quad (16)$$

where Θ_j is defined as

$$\Theta_j \equiv \underbrace{\{C_e^i(j), C_p^i(j), C_e^o(j), C_p^o(j)\}}_c, \underbrace{\{k_{pe}^i, k_{ep}^i, k_{elm}^i, k_{pe}^o, k_{ep}^o, k_{elm}^o\}}_k, \underbrace{\{v_e^i, v_e^o, v_p^i, v_p^o\}}_v, \underbrace{\{x^c, y^c, \theta^c\}}_v. \quad (17)$$

with the assumption that the state equation is exact. The state equation is assumed exact in the sense that we do not consider any process noise. This is why we can express the state at any time instant in terms of the initial state, thus significantly reducing the computational requirements and possible numerical inaccuracies, by using a reduced number of unknowns and not requiring the often difficult tuning of the unknown process noise statistics as in a Kalman filter.

3.3. Measurement equation

Pressure time-series measurements are taken for each measurement time at the detector locations to track the changes in the fluorophore concentration; the time-span of each such pressure time-series being very small compared to the measurement time spacing. At each measurement time, the time domain pressure signal is converted to the frequency domain using discrete Fourier transform. The magnitude spectrum and the frequency spacing in the discrete Fourier transform sequence are used to determine the set of angular frequencies. The range of frequencies considered are based on the Fourier magnitude spectrum of the data, as explained in the numerical studies section. The predicted measurements are obtained by solving the steady state coupled diffusion equation and photoacoustic equation using finite element method in the frequency domain.

The matrix form of the finite element equations for l th frequency is given by

$$\mathbf{A}^l \underline{p}^l = \mathbf{B}^l \underline{h} \quad (18)$$

where the finite element matrices \mathbf{A}^l and \mathbf{B}^l are given in the appendix of [23], for $l = 1 \dots L$, with L being the number of angular frequencies ω_p used.

The discretized heat source \underline{h} is given by:

$$\underline{h} = (\underline{\mu}_{axf} + \underline{\mu}_{axi}) \odot \underline{\Phi}_x + (\underline{\mu}_{amf} + \underline{\mu}_{ami}) \odot \underline{\Phi}_m \quad (19)$$

where the nodal values of the excitation and emission fluences, $\underline{\Phi}_x$ and $\underline{\Phi}_m$, respectively, are calculated using finite element discretization as in [23,39]. Hence the complex pressure

measurements at detectors, \underline{g}^l corresponding to photoacoustic source \underline{h} is given by:

$$\underline{g}^l = \mathcal{D}\underline{p}^l = \mathcal{D}(\mathbf{A}^l)^{-1}\mathbf{B}^l\underline{h} \equiv \mathcal{Z}^l\underline{h} \quad (20)$$

where \mathcal{D} is a $N_D \times N$ matrix (N is the number of discretized nodes) with each row all zeros except for 1 in the column corresponding to a detector location.

The discrete-time measurement equation at time j can thus be written from (20) in terms of the concatenated measurement vector at that time instant \underline{y}_j and the corresponding (concatenated across frequencies) measurement function $\underline{g}_j (= [\underline{g}_j^1; \underline{g}_j^2; \dots; \underline{g}_j^L])$ is given as:

$$\underline{y}_j \equiv \underline{g}_j(\Theta_j) = \underline{g}_j(f_{j-1}(\dots f_0(\Theta_0))) \quad (21)$$

The measurement equation for time instant j and for frequency l can be written as:

$$\underline{g}_j^l(\Theta_j) = \mathcal{Z}^l\underline{h}(\Theta_j) = \mathcal{Z}^l((\underline{\mu}_{axf}(j) + \underline{\mu}_{axi}) \odot \underline{\Phi}_x(j) + (\underline{\mu}_{amf}(j) + \underline{\mu}_{ami}) \odot \underline{\Phi}_m(j)) \quad (22)$$

The unknown states are the compartment-wise fluorophore concentrations and the unknown parameters are the PK-rates and volume fractions. These unknown states and parameters are related to the boundary photoacoustic pressure measurements by the measurement equation as in Equations (21) and (22), with the relation between the concentrations and the absorption coefficients being given as in Equation (14). This clearly defines the relation between the measured photoacoustic pressure on the boundary to the unknown states and parameters. In summary, the PK-FPAT state-variable model consisting of the state-model Equation (15) and the measurement model Equation (21) has now been set up in order to solve for the states ($C_e^i, C_p^i, C_e^o, C_p^o$) and the parameters ($\mathbf{k}, \mathbf{v}, \mathbf{y}$).

The solution of this problem is presented below in two reconstruction schemes, the Jacobian-based GNF and the gradient-based GF. In this work, the state (concentration) and parameter (pharmacokinetic as well as shape parameters) estimation problem is solved using two deterministic schemes, the Jacobian-based GNF [11,31,34] and the gradient-based GF that is introduced in this work.

4. GNF and GF frameworks for RBF level set-based PK-FPAT

4.1. Regularized least-squares problem

The Tikhonov regularized nonlinear least squares problem to be minimized with respect to the parameter of interest, Θ_0 is given by [11,31,34]:

$$\hat{\Theta}_0 = \underset{\Theta_0}{\operatorname{argmin}} \mathcal{F}(\Theta_0) := \frac{1}{2} \|(\mathbf{g}(\Theta_0) - \mathbf{y})\|^2 + \tau \|\Theta_0 - \Theta_c\|^2 \quad (23)$$

where τ is the regularization parameter used with the minimum-norm regularization functional, where Θ_c represents an a priori known constant vector; \mathbf{y} and $\mathbf{g}(\Theta_0)$ are the concatenated set of observed and model-predicted measurements, respectively.

In our work, we have solved the above nonlinear regularized least squares problem in a trust region setting in two frameworks; using a (Jacobian based) Gauss–Newton algorithm to obtain the corresponding GN filter and using a gradient-based scheme to obtain a corresponding filter, that we call the gradient filter (GF). In this section, we now evaluate the

Jacobian and gradient terms that are needed to solve the above least squares problem with GNF and GF schemes, respectively. In the following section, we outline the overall trust region-based optimization schemes used.

4.2. The basic GNF scheme and Jacobian evaluations

The solution to the above minimization problem is first presented with the trust region-based iteratively regularized GN algorithm developed in [11]. A regularized GN update p_Θ solves at the current iterate Θ [11,31,48,49]

$$\hat{p}_\Theta = \underset{p_\Theta}{\operatorname{argmin}} \left\| \frac{\mathbf{J}(\Theta)p_\Theta + \mathbf{r}}{\sqrt{\tau}(\Theta - \Theta_c + p_\Theta)} \right\|^2 \quad (24)$$

where the Jacobian \mathbf{J} and the residual \mathbf{r} are given by

$$\mathbf{J} = \begin{bmatrix} J_0 \\ \vdots \\ J_{M-1} \end{bmatrix}; \quad \mathbf{r} = \begin{bmatrix} r_0 \\ \vdots \\ r_{M-1} \end{bmatrix}; \quad (25)$$

M denotes the number of time instants, Jacobian and residual at time instant j are given by

$$J_j = [J_j^1; J_j^2; \dots; J_j^L]; \quad r_j = [r_j^1; r_j^2; \dots; r_j^L]; \quad (26)$$

The residual at time instant j , for photoacoustic frequency l , is given by

$$r_j^l = g_j^l(\Theta_j) - y_j^l = g_j^l(f_{j-1}(\dots f_0(\Theta_0))) - y_j^l; \quad (27)$$

The Jacobian at time instant j and for photoacoustic signal frequency l is given by:

$$J_j^l = G_j^l[\Theta_j]F_{j-1}[\Theta_j] \dots F_0[\Theta_0] \quad (28)$$

where $G_j^l[\cdot]$ and $F_{j-1}[\cdot]$ are the Jacobian matrices corresponding to measurement $g_j^l(\cdot)$ and state transition $f_{j-1}(\cdot)$ functions, respectively. The $F_{j-1}[\cdot]$ is evaluated as in [11], and the $G_j^l[\cdot]$ is calculated as shown in the following subsection.

4.2.1. Jacobian of measurement function

The Jacobian of the measurement function (20) with respect to the states and parameters at a given time instant j is given by

$$G_j^l = \begin{bmatrix} \underbrace{\frac{\partial g_j^l}{\partial \mathcal{C}(j)}}_{N_D \times 4} & \underbrace{\frac{\partial g_j^l}{\partial k}}_{N_D \times 6} & \underbrace{\frac{\partial g_j^l}{\partial v}}_{N_D \times 4} & \underbrace{\frac{\partial g_j^l}{\partial \gamma}}_{N_D \times 3m} \end{bmatrix} \quad (29)$$

where N_D is the number of detectors. The sensitivity equation with respect to $\alpha \in \{C_e^i(j), C_p^i(j), C_e^o(j), C_p^o(j), k_{pe}^i, k_{ep}^i, k_{elm}^i, k_{pe}^o, k_{ep}^o, k_{elm}^o, v_e^i, v_e^o, v_p^i, v_p^o, x^c, y^c, \theta^c\}$ is calculated using the following chain rule:

$$\frac{\partial g_j^l}{\partial \alpha} = \mathcal{Z}^l \left[\frac{\partial \underline{h}^j}{\partial \underline{\mu}_{axf}^j} \times \frac{\partial \underline{\mu}_{axf}^j}{\partial \alpha} + \frac{\partial \underline{h}^j}{\partial \underline{\mu}_{amf}^j} \times \frac{\partial \underline{\mu}_{amf}^j}{\partial \alpha} \right] \quad (30)$$

with \mathcal{Z}^l and \underline{h}^j being defined in Equation (20) and Equation (19), respectively.

Recalling that $\mu_{amf} = \varepsilon_s \mu_{axf}$, we obtain the derivative of \underline{h}^j with respect to $\underline{\mu}_{axf}^j$ as an $N \times N$ matrix, given by:

$$\frac{\partial \underline{h}^j}{\partial \underline{\mu}_{axf}^j} = \Lambda_x \frac{\partial \underline{\Phi}_x^j}{\partial \mu_{axf}} + \text{diag}(\underline{\Phi}_x^j) + \Lambda_m \frac{\partial \underline{\Phi}_m^j}{\partial \mu_{axf}} + \varepsilon_s \text{diag}(\underline{\Phi}_m^j) \quad (31)$$

where $\Lambda_x = \text{diag}(\underline{\mu}_{axf} + \underline{\mu}_{axi})$, and $\Lambda_m = \text{diag}(\varepsilon_s \underline{\mu}_{axf} + \underline{\mu}_{ami})$.

The sensitivity of the fluence $\underline{\Phi}_m$ and $\underline{\Phi}_x$ with respect to $\underline{\mu}_{axf}$ are evaluated using the adjoint method, where the adjoint fields are calculated with the Dirac source present on all the nodes in the domain.

The sensitivity of μ_{axf} with respect to unknowns Θ can be derived as given in [11]. In the present work, we have used non-compactly supported Hermite interpolation-based RBF representation, the necessary shape derivatives $\frac{\partial s}{\partial \gamma}$ are derived in our earlier work [32].

4.3. Basic GF scheme and gradient evaluation

In order to solve the basic nonlinear least squares problem Equation (23) in a gradient-based setting, we use a quasi-Newton BFGS scheme, which in turn requires the evaluation of gradients of the costfunction. This gradient-based deterministic manner of solution of Equation (23) is called the gradient filter (GF) by us in line with the nomenclature of the Gauss–Newton filter, to solve the state and parameter estimation problem associated with a dynamic state variable model.

We recall that the motivation of using gradient-based schemes stems from the computational complexity of the adjoint problem in the measurement Jacobian-based methods being significantly less than that for the adjoint problem in costfunction-gradient computation [27,28]. The gradients of the least squares FPAT problems in a static setting have been recently derived by us in [27,28]. Here we evaluate the gradient for the regularized least squares formulation of the dynamic PK-FPAT problem.

Consider the Tikhonov regularized least squares problem

$$\mathcal{F}(\Theta_0) = \frac{1}{2} \|(\mathbf{g}(\Theta_0) - \mathbf{y})\|^2 + \tau \|\Theta_0 - \Theta_c\|^2 \quad (32)$$

$$= \frac{1}{2} \left(r_0^T r_0 + r_1^T r_1 + \dots + r_{M-1}^T r_{M-1} \right) + \tau \|\Theta_0 - \Theta_c\|^2 \quad (33)$$

The gradient of this cost function is given by

$$\mathcal{G} = \frac{\partial \mathcal{F}}{\partial \Theta_0} = \left(\frac{\partial r_0}{\partial \Theta_0} \right)^T r_0 + \dots + \left(\frac{\partial r_{M-1}}{\partial \Theta_0} \right)^T r_{M-1} + 2\tau (\Theta_0 - \Theta_c) \quad (34)$$

$$= \mathcal{G}_0 + \dots + \mathcal{G}_{M-1} + 2\tau (\Theta_0 - \Theta_c) \quad (35)$$

The derivatives of the measurement residuals at various time instants with respect to Θ_0 is given as

$$\frac{\partial r_j}{\partial \Theta_0} = \frac{\partial g_j}{\partial \Theta_0} = G_j[\Theta_j] F_{j-1}[\Theta_{j-1}] \dots F_0[\Theta_0] \quad (36)$$

Denoting $G_j \equiv [G_j^1; G_j^2; \dots; G_j^L]$, where the G_j^l , $l = 1 \dots L$, are defined in Equation (29), we can write

$$G_j = \mathcal{Z} \frac{\partial \underline{h}^j}{\partial \underline{\mu}_{axf}^j} \frac{\partial \underline{\mu}_{axf}^j}{\partial \Theta_j} \quad (37)$$

where $\mathcal{Z} = [\mathcal{Z}^1; \mathcal{Z}^2; \dots; \mathcal{Z}^L]$, where the \mathcal{Z}^l , $l = 1 \dots L$, are defined in Equation (20).

The gradient term for time instant j in Equation (35) can thus be written as

$$\begin{aligned} \left(\frac{\partial g_j}{\partial \Theta_0} \right)^T r_j &= (F_0[\Theta_0])^T \dots (F_{j-1}[\Theta_{j-1}])^T (G_j[\Theta_j])^T r_j \\ &= (F_0[\Theta_0])^T \dots (F_{j-1}[\Theta_{j-1}])^T \left(\frac{\partial \underline{\mu}_{axf}^j}{\partial \Theta_j} \right)^T \left(\frac{\partial \underline{h}^j}{\partial \underline{\mu}_{axf}^j} \right)^T (\mathcal{Z})^T r_j \end{aligned} \quad (38)$$

In the above equation, for ease of notation, denote the vector $(\mathcal{Z})^T r_j \equiv R_j$. Using Equation (31), the last three terms can be written as

$$\begin{aligned} \left(\frac{\partial \underline{h}^j}{\partial \underline{\mu}_{axf}^j} \right)^T R_j &= \overbrace{\left(\frac{\partial \underline{\Phi}_x^j}{\partial \underline{\mu}_{axf}^j} \right)^T \Lambda_x R_j + \text{diag}(\underline{\Phi}_x^j)^T R_j}^{T1} + \overbrace{\left(\frac{\partial \underline{\Phi}_m^j}{\partial \underline{\mu}_{axf}^j} \right)^T \Lambda_m R_j}^{T2} \\ &\quad + \varepsilon_s \left(\text{diag}(\underline{\Phi}_m^j) \right)^T R_j \end{aligned} \quad (39)$$

where, the derivatives of $\underline{\Phi}_x^j$ and $\underline{\Phi}_m^j$ with respect to $\underline{\mu}_{axf}^j$ (summarized in Appendix 1) are calculated from the sensitivity relations [39] using the method of adjoints, and are given by

$$\frac{\partial \underline{\Phi}_x^j}{\partial \underline{\mu}_{axf}^j} = -\Psi_{xx}^T \mathbf{A}_x^{\mu,i} \Phi_x \equiv -\Psi_{xx}^T \mathbf{a}_x^{\mu,i} \quad (40)$$

$$\begin{aligned} \frac{\partial \underline{\Phi}_m^j}{\partial \underline{\mu}_{axf}^j} &= -\Psi_{xm}^T \mathbf{A}_x^{\mu,i} \Phi_x - \Psi_{mm}^T \mathbf{A}_m^{\mu,i} \Phi_m + \Psi_{mm}^T \mathbf{M}_{\beta}^{\mu,i} \Phi_x \\ &\equiv -\Psi_{xm}^T \mathbf{a}_x^{\mu,i} - \Psi_{mm}^T \mathbf{a}_m^{\mu,i} + \Psi_{mm}^T \mathbf{m}_{\beta,x}^{\mu,i} \end{aligned} \quad (41)$$

where Ψ_{xx} , Ψ_{xm} and Ψ_{mm} are the solutions to the adjoint system of equations (Equation (A1) in Appendix 1).

Denoting $\tilde{\mathbf{A}}_{x/m}^{\mu} = [\mathbf{a}_{x/m}^{\mu,1} \dots \mathbf{a}_{x/m}^{\mu,N}]$, we use Equation (40) to write term T1 of Equation (39) as

$$\left(\frac{\partial \underline{\Phi}_x^j}{\partial \underline{\mu}_{axf}^j} \right)^T \Lambda_x R_j = -(\tilde{\mathbf{A}}_x^{\mu})^T \underbrace{\Psi_{xx} \Lambda_x R_j}_{\tilde{\Psi}_{xx}} \quad (42)$$

Using Equation (41), term $T2$ of Equation (39) can be written as

$$\left(\frac{\partial \Phi_m^j}{\partial \mu_{axf}} \right)^T \Lambda_m R_j = -(\tilde{\mathbf{A}}_x^\mu)^T \underbrace{\Psi_{xm} \Lambda_m R_j}_{\tilde{\Psi}_{xm}} - (\tilde{\mathbf{A}}_m^\mu)^T \underbrace{\Psi_{mm} \Lambda_m R_j}_{\tilde{\Psi}_{mm}} + (\tilde{\mathbf{M}}_{\beta,x}^\mu)^T \underbrace{\Psi_{mm} \Lambda_m R_j}_{\tilde{\Psi}_{mm}} \quad (43)$$

where $\tilde{\mathbf{M}}_{\beta,x}^\mu = [\mathbf{m}_{\beta,x}^{\mu,1} \cdots \mathbf{m}_{\beta,x}^{\mu,N}]$.

Thus, from Equation (A1) of Appendix 1, $\tilde{\Psi}_{xx}$, $\tilde{\Psi}_{mm}$ and $\tilde{\Psi}_{xm}$ are obtained by solving the following equations

$$\mathbf{A}_x \tilde{\Psi}_{xx} = \Lambda_x^T R_j; \quad \mathbf{A}_m \tilde{\Psi}_{mm} = \Lambda_m^T R_j; \quad \mathbf{A}_x \tilde{\Psi}_{xm} = \mathbf{M}_\beta \tilde{\Psi}_{mm} \quad (44)$$

Thus, to summarize, we first calculate adjoint vectors $\tilde{\Psi}_{xx}$, $\tilde{\Psi}_{xm}$ and $\tilde{\Psi}_{mm}$ from Equation (44). Next step is to calculate the terms $T1$ and $T2$ as in Equation (39) and substitute the terms into Equation (38) to calculate the gradient for time instant j , and thus obtain the cost-function gradient from Equation (35).

The main difference in the gradient calculation from the Jacobian one, is that we don't have to solve for adjoint matrices Ψ_{xx} , Ψ_{xm} and Ψ_{mm} as needed for the Jacobian, but only for the adjoint vectors $\tilde{\Psi}_{xx}$, $\tilde{\Psi}_{xm}$ and $\tilde{\Psi}_{mm}$. Hence the memory and computational requirements in the implementation of the gradient calculation is much lesser as compared to that of a Jacobian.

5. Reconstruction algorithms

In this section we outline the specific algorithmic approaches for the GNF and GF used to solve the dynamic PK-FPAT reconstruction. The GN-filter reconstruction algorithm solves a succession of linearized least-squares subproblems (24), in a trust region-based iteratively regularized GN algorithm developed in [11]; we do not repeat the algorithmic details here for the sake of brevity. In the rest of this section, we present our proposed trust region-based gradient filter reconstruction algorithm.

5.1. Regularized trust region-based GF

The GF reconstruction algorithm solves the minimization problem (23) using a trust region-based iteratively regularized BFGS scheme. We use the following quasi-Newton BFGS update [50]

$$\mathbf{B}^{(i+1)} = \mathbf{B}^{(i)} - \frac{\mathbf{B}^{(i)} \underline{s}^{(i)} \underline{s}^{(i)T} \mathbf{B}^{(i)T}}{\underline{s}^{(i)T} \mathbf{B}^{(i)} \underline{s}^{(i)}} + \frac{\underline{y}^{(i)} \underline{y}^{(i)T}}{\underline{y}^{(i)T} \underline{s}^{(i)}} \quad (45)$$

with $\underline{s}^{(i)} = p_\Theta$ and $\underline{y}^{(i)} = \mathcal{G}^{(i+1)} - \mathcal{G}^{(i)}$. p_Θ is the trust region update calculated by solving the following equation

$$(\tilde{\mathbf{B}}_a + \lambda I) \tilde{p}_\Theta = -\tilde{\mathcal{G}} \quad (46)$$

$$p_\Theta = S \cdot \tilde{p}_\Theta \quad (47)$$

where $\tilde{\mathbf{B}}_a$ is the scaled version of the augmented Hessian $\mathbf{B}_a (= \mathbf{B} + \tau I)$; $\tilde{\mathbf{B}}_a = S^T \cdot \mathbf{B}_a \cdot S$, with S being a scaling matrix defined below. The scaled version of the gradient is

$\tilde{\mathcal{G}} = S^T \cdot \mathcal{G}$. S is a diagonal scaling matrix used to keep the solution update more balanced [50]. The elements in the scaling matrix used in our work are [49]

$$S_{ii} = \frac{1}{\sqrt{|\mathbf{B}_{ii}| + \tau}} \quad (48)$$

Parameter λ is calculated by solving the following equation using a suitable root finding technique [50,51]

$$\|\tilde{p}_{\Theta_0}\| = \Delta = \|(\tilde{\mathbf{B}}_a + \lambda I)^{-1} \tilde{\mathcal{G}}\|_2 \quad (49)$$

where Δ is the trust region radius.

We use an iterative regularization scheme in the spirit of our work in [48], here in a trust region framework (as introduced by us in [11]). τ is the iterative regularization parameter, whose value is decreased to τ/q ($q > 1$) in the next iteration if a ‘good step’ is taken as per the trust region update; a trust region step is considered ‘good’ when the reduction ratio parameter (ratio of actual to predicted reductions in cost functions) is greater than a specified threshold (in our work, we have used a threshold value of 1.0). In our computational experience, we have observed that $q = 3$ gives us the adequate balance between responding to a good trust region step, and not reducing the regularization parameter too fast (that will potentially affect the global convergence of the algorithm).

The stopping criterion employed is to check whether the magnitude of the gradient is low enough or the estimates are stable across iterates. We outline the regularized trust region-based gradient filter in the flow chart shown in ‘Algorithm 1’

The algorithmic parameters η_1 , η_2 , $\Delta_0 = 1$ and the trust region updating rule in Algorithm 1 are based on the practical trust region algorithm suggested in Conn et al. [52].

6. Numerical studies

6.1. Test cases and reconstructions

A square computational domain of size $[-5 \text{ mm}, 5 \text{ mm}] \times [-5 \text{ mm}, 5 \text{ mm}]$ as considered in [53] is taken for numerical test cases. Four laser pulse sources (1 J/mm^2) are placed at the centre of each side and 40 detectors, separated by 1 mm, are placed on the four sides of the boundary, with four at the corners and the remaining 36 on the sides as shown in Figure 2. The intrinsic absorption coefficients, μ_{axi} and μ_{ami} are time invariant and are assumed known in our work since our objective is to study the behaviour of the reconstructions of the fluorescence parameter μ_{axf} ; in principle μ_{axi} and μ_{ami} can be reconstructed using quantitative photoacoustic tomography [27,54,55] at excitation and emission wavelengths. Considering the robustness of FPAT reconstructions to perturbations of the assumed background from the actual value (as demonstrated in [27]), without loss of generality and for clarity of focus of the present paper, we consider a known homogeneous background in our present numerical studies. We recall that FPAT comes into the picture when high quantum efficiency contrast agents ensure the fluorescence-contribution to the photoacoustic heat source is significant [23].

Assuming the intrinsic coefficients to be homogeneous (the limiting case of low contrast in intrinsic chromophore properties), the optical properties used for the

Algorithm 1 Trust region-based iteratively regularized GF

```

1: Initialization:  $\Theta^0, \Theta_c = \Theta^0, \mathbf{B} = \mathbf{I}, \Delta_0, \eta_1 = 0.01, \eta_2 = 0.9, \tau_0 = 0.8, i = 0$ 
2: Calculate  $\mathcal{G}^0$  using  $\Theta^0$ 
3: while  $i < i_{max}$  do
4:   calculate  $\lambda$  using (49)
5:   solve for  $p_\Theta$  using (47)
6:    $\Theta^t = \Theta^i + p_\Theta$ 
7:   Evaluate  $\mathcal{F}(\Theta^t)$  and  $\rho = \frac{\mathcal{F}(\Theta^t) - \mathcal{F}(\Theta^i)}{-(p_\Theta^T \mathcal{G}^i + 0.5 * p_\Theta^T \mathbf{B}_a p_\Theta)}$ 
8:   if  $\rho > \eta_1$  then
9:     Accept update.  $\Theta^{i+1} = \Theta^t$ ;
10:    if  $\rho > \rho_{th}$  then
11:       $\tau_{i+1} = \max(\tau_i/3, \tau_{min})$ ;
12:    end if
13:  else
14:     $\Theta^{i+1} = \Theta^i$ ;
15:  end if
16:
17:  if  $\rho > \eta_2$  then
18:     $\Delta_{i+1} = \max(2.5 \cdot \|p_\Theta\|, \Delta_i)$ ;
19:  else if  $\rho \geq \eta_1 \& \rho < \eta_2$  then
20:     $\Delta_{i+1} = \Delta_i$ ;
21:  else if  $\rho \geq 0 \& \rho < \eta_1$  then
22:     $\Delta_{i+1} = 0.25 \cdot \|p_\Theta\|$ ;
23:  else if  $\rho < 0$  then
24:     $\Delta_{i+1} = \min(0.25 \cdot \|p_\Theta\|, \max(0.0625, \gamma_{bad}) \cdot \Delta_i)$ ;
25:  end if
26:
27:  Calculate  $\mathcal{G}^{i+1}$  using  $\Theta^{i+1}$ 
28:  update  $\mathbf{B}$  using Equation (45)
29:   $i = i + 1$ ;
30: end while
31: Choose the stopping iterate when  $|\mathcal{G}| < tol$ , or, the data-residual staying stable or
    toggling across iterations.

```

phantom are [23,41]: $\mu_{axi} = 0.0031 \text{ mm}^{-1}$, $\mu_{ami} = 0.00415 \text{ mm}^{-1}$, $\mu'_{sx} = 1.095 \text{ mm}^{-1}$, $\mu'_{sm} = .929 \text{ mm}^{-1}$, $\tau = 0.56 \text{ ns}$, $\phi_q = 0.4$, $R_{x,m} = 0.431$, $\epsilon_x = 13000 \text{ M}^{-1} \text{ mm}^{-1}$, $\epsilon_m = 1100 \text{ M}^{-1} \text{ mm}^{-1}$. The homogeneous acoustic properties are [56] $\beta = 4 \times 10^{-4} \text{ K}^{-1}$, $C^p = 4000 \text{ J Kg}^{-1} \text{ K}^{-1}$.

The pharmacokinetic rates mentioned for invasive ductal carcinoma (IDC) and adenocarcinoma (AC) from [10] are used to generate measurement data. In the data generation, at first time instant, the concentration of the fluorophore is assumed to be $6.5 \mu\text{M}$ in the plasma compartment and $0 \mu\text{M}$ in the EES compartment.

Numerical studies are performed for two phantoms in two cancer-types (IDC and AC). A two-object phantom (denoted by ‘T’) contains two adjacently-placed objects with each

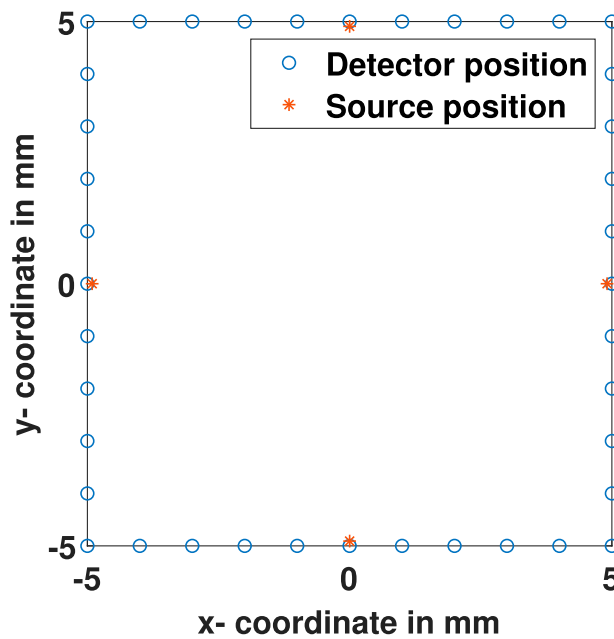


Figure 2. Schematic representation source and detector setting for the numerical study.

Table 1. SNR of the synthetic data.

SNR	T Phantom		B Phantom	
	IDC	AC	IDC	AC
40	I-T1	A-T1	I-B1	A-B1
30	I-T2	A-T2	I-B2	A-B2
25	I-T3	A-T3	I-B3	A-B3
20	I-T4	A-T4	I-B4	A-B4

having approximate extent of 1.6 mm in each direction and their boundaries separated by approximately 2.4 mm. The bean phantom, (denoted by ‘B’) is a single bean shape object with lateral and longitudinal extents being approximately 2 and 3.2 mm, respectively. Data is generated for the two phantoms at three SNR levels by adding noise to the discrete time sequence of the measurements using the *awgn* command in MATLAB; we have given it in Table 1.

The data is generated using finite element solutions of the forward model on a finer mesh discretized with 40,401 nodes containing 80,000 triangular elements. Jacobian and gradient-based reconstructions are performed with the same data sets on a coarser mesh discretized with 10,201 nodes containing 20,000 triangular elements.

Considering the close correspondence of our frequency domain finite element method and the time-domain *k*-wave toolbox [57] solvers for the photoacoustic equation, the frequency spacing and the range of frequencies used in solving the frequency domain photoacoustic equation is determined from time domain data generated using the *k*-wave toolbox in the same computational setting. A plot of the discrete Fourier transform magnitude spectrum calculated from the *k*-wave data showed a significant portion to be within 1 MHz. Hence we considered frequency content below 1 MHz. Let T_s be the size of the time

step and the N_s be the number of time samples generated using k -wave for the resolution and the domain size considered, then the frequency spacing, $\Delta\Omega_s$ is calculated using the frequency scaling relation [58]:

$$\omega_s = \Omega_s T_s \Rightarrow \Delta\Omega_s = \frac{\Delta\omega_s}{T_s} = \frac{2\pi}{N_s T_s} \quad (50)$$

where $\Delta\omega_s$ comes from the discrete Fourier transform frequency spacing relation [58]: $\Delta\omega_s = \frac{2\pi}{N_s}$. $\Delta\Omega_s$ turns out to be around 100 KHz for the given settings. Hence the pressure fields are generated by solving the photoacoustic equation using finite element method for 10 equispaced frequencies between 2.5 KHz to 902.5 KHz. A brief discussion of literature corresponding to photoacoustic tomography systems with respect to similar abnormality-sizes and corresponding frequency selection aspects can found in our earlier work [28].

Data is collected at a sampling interval of 5sec for 40 time instants in a two object phantom and 80 time instants for the bean phantom. At each time instant, one source is on and measurements are taken on all detectors. The measurements are amplified by 60 dB as in [59]. All the computations are performed in the Matlab[®] 2019a programming environment run on the HPC facility at IIT Kanpur. We use our HPC cluster to run the algorithms simultaneously for different test cases. The data generation and the reconstructions are performed on the HPC. Each node in the HPC cluster has 128 GB RAM (or a high memory node with 768 GB RAM) and 20 cores for parallel processing. On each node of the HPC, we have used the parallel computing toolbox from the MATLAB[®] to evaluate Jacobians and gradients at different time instants simultaneously. We use a 128 GB RAM workstation only to show the comparison of the execution time of a Jacobian (240 sec per measurement time instant) and the gradient (4 sec per measurement time instant, and about 25 sec per iteration for 40 time instants evaluated in two lots of 20) computations.

The Jacobian-based algorithm is also run on a high memory node (with 768 GB RAM) of the HPC cluster. The execution time of a 20 time instant Jacobian evaluation on the high memory node using 20 parallel workers is approximately 890 seconds (approximately 15 minutes). The total time for Jacobian evaluation for one iteration (in the case of a bean with data from 80 time instants) is approximately 60 minutes; one iteration of the Jacobian-based reconstruction has taken usually between 60–70 minutes. The Jacobian-based reconstruction algorithm typically converges in 30–50 iterations.

We have found that the time taken for gradient calculation per iteration in the gradient-based algorithm to be of the order of 25 seconds. The order of time taken for a typical gradient-based reconstruction is around an hour for 100 iterations; reconstructions converge in about 100–120 iterations in our experience. Further, next level code-optimization by way of a use of more cores or using CPU-GPU frameworks and speeding up specific units such as the finite element global assembly and adjoint evaluations, is expected to yield further significant reductions in the computational time taken per iteration to a fraction of the existing times, and hence the whole reconstruction too.

In order to get an idea of the relative computation times of our dynamic quantitative FPAT reconstructions with respect to static qualitative QPAT reconstruction, we have checked the time taken for the heat source reconstruction using the adjoint-based iterative PAT reconstruction of the k -wave toolbox. We note that for a typical test case parameter set considered in our work, for one time instant, the time taken by the above mentioned adjoint-based iterative solver on our 128 GB system is of the order of 30 seconds (typically

needed about five iterations to converge). This in our opinion compares reasonably with our fully nonlinear gradient filter scheme taking about 25 seconds for a gradient computation and about 35 seconds per reconstruction-iteration (and about an hour and a quarter for the about 100–120 iterations typically required), especially with the further avenues of significant speed-up as discussed above.

Initial fluorophore concentration in plasma compartment is assumed to be the injected concentration and concentration of the fluorophore in EES compartment is assumed to be zero as considered in [35,60]. In both the schemes, the starting estimates for pharmacokinetic rates are taken in between approximate healthy and tumour values corresponding to IDC. v_e and v_p are initialized approximately with healthy tissue values. For the RBF level-set representation in the Jacobian iterative scheme, we use six and five centres, respectively, for the two object and bean phantoms. In the gradient-based iterative scheme we used six RBF centres for the level-set representation in both the phantoms. We have used the least number of centres that have yielded closed curves in the reconstructions.

The reconstructed pharmacokinetic parameter values from the GN-filter scheme for IDC and AC cases are given in Tables 2 and 4, respectively. The reconstructed values of the pharmacokinetic parameters from the gradient filter for IDC and AC cases are given in Tables 3 and 5, respectively. Figures 3 and 5 contain the GN-filter scheme reconstructions for IDC and AC cases, respectively. Figures 4 and 6 contain the gradient filter scheme reconstructions for IDC and AC cases, respectively. In the figures, the shape reconstructions (with the RBF-centres being marked as stars) are shown in the first column, second and third columns contain the concentration curves inside and outside the tumour region, respectively. We restrict the figures to the datasets with SNRs of 30 dB and 20 dB for brevity without loss of information.

The numerical studies show a good localization in the shape reconstruction results. The pharmacokinetic transfer rates and volumes fractions show reasonable contrast to differentiate healthy and tumourous tissue. We have observed that the reconstruction results for a two object phantom using data from 80 time instants are similar to the results from 40 time instants. In the case of a bean phantom, the results are better using data from 80 time instants (compared to 40 time instants).

Table 2. Pharmacokinetic reconstructions for invasive ductal carcinoma (IDC) test cases using GN-filter.

Parameter	True values	Reconstructed values							
		I-T1	I-T2	I-T3	I-T4	I-B1	I-B2	I-B3	I-B4
C_e^i	0	0.0044	0.0046	0.0043	0.0044	0.0032	0.0032	0.0031	0.0033
C_e^o	0	6.7×10^{-7}	6.4×10^{-7}	3.1×10^{-7}	7.1×10^{-7}	3.2×10^{-6}	2.8×10^{-6}	4.7×10^{-6}	2.3×10^{-6}
C_p	6.5	6.5	6.5	6.5	6.5	6.5	6.5	6.5	6.5
C_p^o	6.5	6.5	6.5	6.5	6.5	6.5	6.5	6.5	6.5
k_{pe}^i	0.0687	0.0877	0.0874	0.0869	0.0863	0.0693	0.0692	0.0697	0.0688
k_{pe}^o	0.0306	0.0311	0.0310	0.0307	0.0308	0.0322	0.0323	0.0328	0.0315
k_{ep}^i	0.0496	0.0260	0.0258	0.0258	0.0256	0.0208	0.0207	0.0210	0.0204
k_{ep}^o	0.0166	0.0160	0.0162	0.0165	0.0163	0.0152	0.0150	0.0148	0.0157
k_{elm}^i	0.00449	0.0070	0.0070	0.0070	0.0070	0.0070	0.0070	0.0070	0.0070
k_{elm}^o	0.00446	0.0047	0.0047	0.0047	0.0049	0.0049	0.0049	0.0050	0.0046
v_e^i	0.3	0.2488	0.2490	0.2498	0.2506	0.1962	0.1964	0.1961	0.1969
v_e^o	0	4×10^{-4}	3.7×10^{-4}	2.4×10^{-4}	4.9×10^{-4}	0.0017	0.0018	0.0019	0.0014
v_p^i	0.0600	0.0597	0.0594	0.0592	0.0586	0.0513	0.0512	0.0509	0.0508
v_p^o	0.0200	0.0200	0.0199	0.0198	0.0197	0.0200	0.0200	0.0200	0.0198

Table 3. Pharmacokinetic reconstructions for invasive ductal carcinoma (IDC) test cases using gradient filter.

Parameter	True values	Reconstructed values							
		I-T1	I-T2	I-T3	I-T4	I-B1	I-B2	I-B3	I-B4
C_e^i	0	0.01	0.01	0.01	0.01	0.01	0.01	0.01	0.01
C_e^o	0	0.01	0	0.0035	0.0099	0.01	3.5×10^{-5}	0.0096	6.7×10^{-4}
C_p	6.5	6.5	6.5	6.5	6.5	6.5	6.5	6.5	6.5
C_p^o	6.5	6.48	6.49	6.5	6.45	6.43	6.5	6.5	6.49
k_{pe}^i	0.0687	0.0859	0.0754	0.0826	0.0847	0.0845	0.0695	0.0743	0.0721
k_{pe}^o	0.0306	0.0316	0.0335	0.0327	0.0304	0.0309	0.0332	0.0316	0.0315
k_{ep}^i	0.0496	0.0314	0.0281	0.0310	0.0313	0.0258	0.0238	0.0249	0.0246
k_{ep}^o	0.0166	0.0135	0.0117	0.0134	0.0171	0.0112	0.0135	0.0164	0.0156
k_{elm}^i	0.00449	0.0070	0.0070	0.0070	0.0070	0.0070	0.0070	0.0070	0.0070
k_{elm}^o	0.00446	0.0039	0.0060	0.0056	0.0047	0.0048	0.0054	0.0045	0.0046
v_e^i	0.3	0.2537	0.2567	0.2573	0.2568	0.1862	0.1970	0.1961	0.1981
v_e^o	0	8×10^{-4}	0.0028	0.0020	1.1×10^{-5}	0.0025	0.0026	9.2×10^{-4}	0.0014
v_p^i	0.0600	0.0593	0.0650	0.0593	0.0579	0.0517	0.0501	0.0496	0.0493
v_p^o	0.0200	0.0199	0.0200	0.0198	0.0199	0.0200	0.0200	0.0200	0.0198

Table 4. Pharmacokinetic reconstructions for Adenocarcinoma (AC) test cases using GN-filter.

Parameter	True values	Reconstructed values							
		A-T1	A-T2	A-T3	A-T4	A-B1	A-B2	A-B3	A-B4
C_e^i	0	0.0028	0.0026	0.0026	0.0027	0.0019	0.0019	0.0020	0.0018
C_e^o	0	0	1.2×10^{-7}	0	0	0	0	0	0
C_p	6.5	6.5	6.5	6.5	6.5	6.5	6.5	6.5	6.5
C_p^o	6.5	6.5	6.5	6.5	6.5	6.5	6.5	6.5	6.5
k_{pe}^i	0.0292	0.0326	0.0327	0.0329	0.0331	0.0275	0.0277	0.0279	0.0282
k_{pe}^o	0.0114	0.0114	0.0113	0.0112	0.0111	0.0113	0.0113	0.0113	0.0112
k_{ep}^i	0.0158	0.0096	0.0096	0.0096	0.0096	0.0086	0.0086	0.0086	0.0086
k_{ep}^o	0.0065	0.0065	0.0065	0.0064	0.0064	0.0070	0.0069	0.0068	0.0067
k_{elm}^i	0.0043	0.0070	0.0070	0.0070	0.0070	0.0061	0.0061	0.0061	0.0062
k_{elm}^o	0.0035	0.0036	0.0035	0.0036	0.0035	0.0033	0.0033	0.0032	0.0031
v_e^i	0.2000	0.1861	0.1862	0.1863	0.1864	0.1467	0.1467	0.1466	0.1467
v_e^o	0	0	0	9.6×10^{-5}	0	0	0	0	0
v_p^i	0.0400	0.0397	0.0394	0.0390	0.0383	0.0366	0.0364	0.0362	0.0358
v_p^o	0.0200	0.0200	0.0199	0.0199	0.0198	0.0200	0.0200	0.0199	0.0198

In our work we have used the triharmonic basic function as a non-compactly supported RBF, along with a quadratic polynomial term [48]. We observe that using the non-compactly supported RBF needs much fewer centres and yields a better ability to completely enclose the shape of concave shaped objects than the compactly supported RBFs used in [11].

We observe that the reconstruction results of the shapes and pharmacokinetic parameters from the GF are as good as the results from the GNF with the same data and mesh resolution. The size of the Hessian matrix involved in the BFGS update is quite small (32×32 , the unknown vector has 14 components for the pharmacokinetic parameters, and 18 for the six RBF centres (x, y, θ)) owing to the level-set representation. As the Jacobian-based scheme becomes computationally heavy for large number of nodes in the domain due to memory and time constraints, the gradient-based scheme is a practically realistic method for the PK-FPAT problem.

Table 5. Pharmacokinetic reconstructions for Adenocarcinoma (AC) test cases using gradient filter.

Parameter	True values	Reconstructed values							
		A-T1	A-T2	A-T3	A-T4	A-B1	A-B2	A-B3	A-B4
C_e^i	0	0.01	0.01	0.01	0.01	0.01	0.01	0.0045	0.0062
C_e^o	0	0.0064	0.01	3.5×10^{-5}	0.0035	0	9.5×10^{-5}	0	0
C_p^i	6.5	6.5	6.5	6.5	6.5	6.5	6.5	6.5	6.5
C_p^o	6.5	6.48	6.5	6.48	6.49	6.5	6.49	6.5	6.5
k_{pe}^i	0.0292	0.0366	0.0361	0.0372	0.0371	0.0305	0.0334	0.0284	0.0313
k_{pe}^o	0.0114	0.0117	0.0122	0.0115	0.0113	0.0117	0.0120	0.0119	0.0114
k_{ep}^i	0.0158	0.0093	0.0093	0.0104	0.0094	0.0083	0.0085	0.0082	0.0090
k_{ep}^o	0.0065	0.0060	0.0054	0.0060	0.0060	0.0062	0.0050	0.0054	0.0065
k_{elm}^i	0.0043	0.0070	0.0070	0.0062	0.0070	0.0065	0.0066	0.0064	0.0061
k_{elm}^o	0.0035	0.0032	0.0024	0.0031	0.0032	0.0037	0.0052	0.0041	0.0033
v_e^i	0.2000	0.1762	0.1782	0.1759	0.1767	0.1423	0.1375	0.1425	0.1328
v_e^o	0	1.2×10^{-4}	1.1×10^{-5}	3.3×10^{-5}	7.4×10^{-5}	0.0013	0.0040	0.0023	1.5×10^{-4}
v_p^i	0.0400	0.0381	0.0380	0.0372	0.0366	0.0352	0.0341	0.0356	0.0335
v_p^o	0.0200	0.0200	0.0199	0.0199	0.0197	0.0200	0.0200	0.0199	0.0198

The Jacobian matrix is computed using a vectorized implementation in the spirit of the seminal paper of Fedele et al. [39]. The gradient computations could be run for 20 time instants simultaneously on a single node using parallel computing toolbox, where as the Jacobian computations could be run for only 4 time instants simultaneously due to memory constraints. As the number of nodes increases the GNF becomes much more difficult to implement as compared to the gradient filter. On the other hand, the GNF generally takes less iterations (in the range of 30–50 in the test cases considered) compared to gradient filter (in the range of around 100–120).

6.2. Error quantification

The quality of the shape and parameter reconstructions is quantified by the following four error measures (as in ref. [11]): normalized error of area-parameter product across time instants (E_{AP}), the distance of the centroid of the reconstructed object from the actual object (E_C), the Dice coefficient for the shape reconstructions ($D(U, V)$), and normalized mean square error (NMSE) for the pharmacokinetic rates. These error metrics are defined in [11]. The definition has been repeated in Appendix 2 to ensure readability. The reconstructed shape and the pharmacokinetic rates are mapped spatially using (11) to calculate NMSE (in dB) for pointwise evaluated pharmacokinetic rates and volume fraction images. This image quality metric is used to compare the results with the existing literature [9,11].

The NMSE defined for a reconstructed quantity \mathbf{X}^r with respect to its actual value \mathbf{X}^a is defined as

$$E_{\text{NMSE}} = \frac{\|\mathbf{X}^r - \mathbf{X}^a\|^2}{\|\mathbf{X}^a\|^2} \quad (51)$$

The metric $E_{\text{NMSE}}(\mathbf{k})$, is evaluated for the concatenated vector \mathbf{k} (the vector being defined in Equation (17)) as shown in Equation (17). The error metrics evaluated for the numerical test cases at different noise levels are tabulated in tables 6 and 7. The error metrics E_C and $D(U, V)$ demonstrate the localization in the shape results. The metrics E_{AP} and E_{NMSE} show the reasonable reconstruction in the shape and parameter values. The NMSE (in dB)

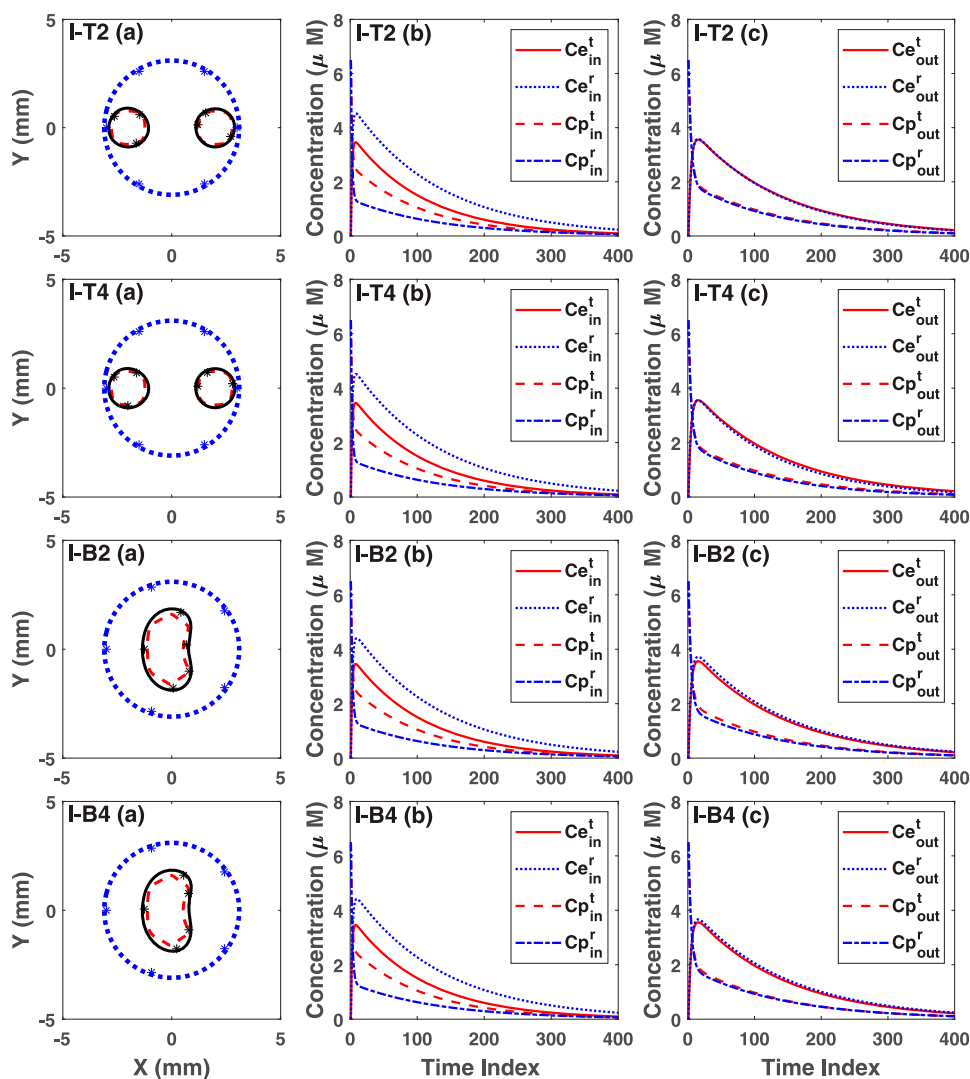


Figure 3. Jacobian-based reconstruction of two object and bean phantoms (labelled (a)), and concentration vs time plot (labelled (b), (c)) in IDC tumour; (top-to-down: data-sets I-T2, I-T4, I-B2, I-B4) In the left column (a), blue dotted line denotes the initial level-set, red dashed line denotes the shape of true object, and solid black line denotes the reconstructed shape. In the 2nd and 3rd columns, red denotes the decay of concentration in true phantom (with superscript t) and blue denotes the decay in reconstructed phantom (with superscript r). The 2nd column shows C_e and C_p plots inside the tumour region. The 3rd column shows C_e and C_p plots outside the tumour region. 1 time-index = 5 seconds.

of the pointwise maps for the pharmacokinetic rates and volume fractions are tabulated in Tables 8 and 9.

6.3. Comparison with PK-FOT results

We now discuss the performance of our PK-FPAT formulations with respect to earlier PK-FOT formulations with GN-filter [11] and point-wise Kalman filter-based solutions [9].

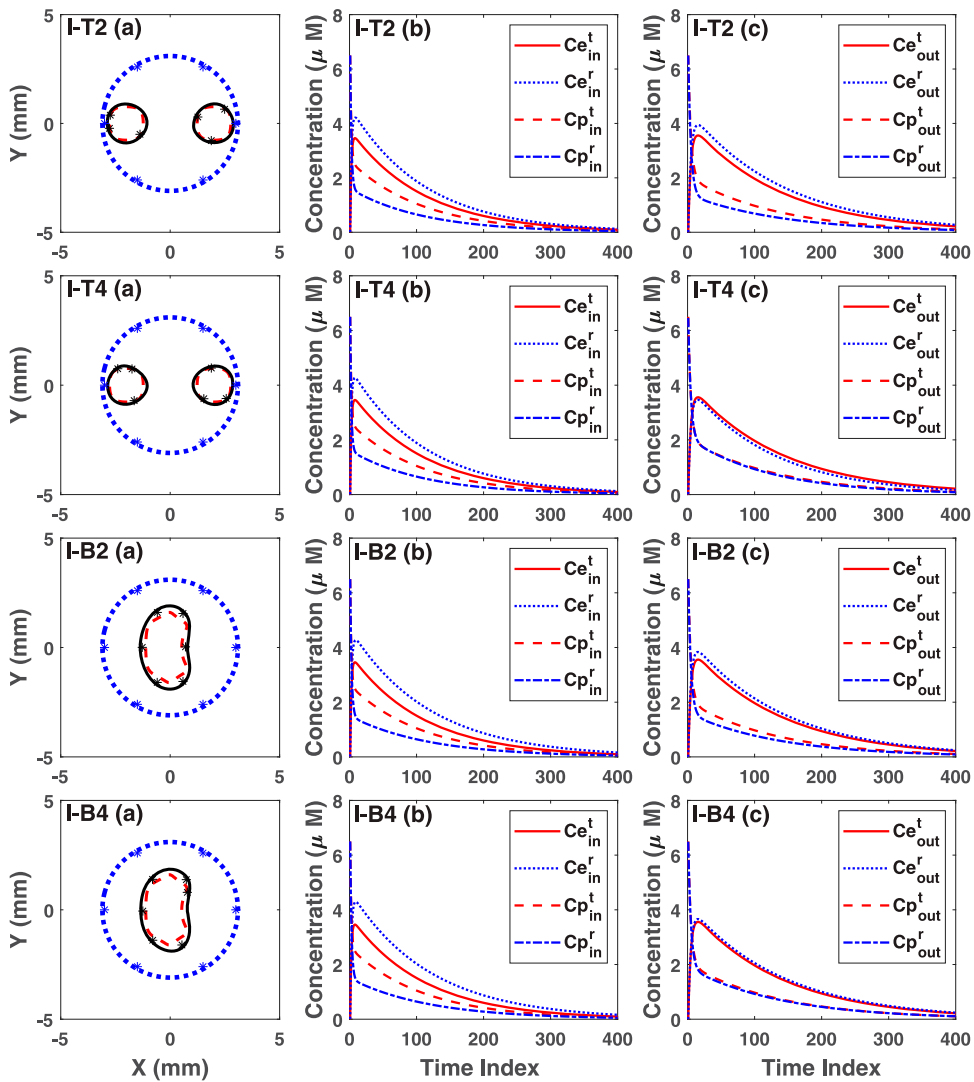


Figure 4. Gradient-based reconstruction of two object and bean phantoms (labelled (a)), and concentration vs time plot (labelled (b), (c)) in IDC tumour; (top-to-down: data-sets I-T2, I-T4, I-B2, I-B4) In the left column (a), blue dotted line denotes the initial level-set, red dashed line denotes the shape of true object, and solid black line denotes the reconstructed shape. In the 2nd and 3rd columns, red denotes the decay of concentration in true phantom (with superscript t) and blue denotes the decay in reconstructed phantom (with superscript r). The 2nd column shows C_e and C_p plots inside the tumour region. The 3rd column shows C_e and C_p plots outside the tumour region. 1 time-index = 5 seconds.

We do not compare our reconstructions with DCE-MSOT formulations such as in [17], since (a) their single-ODE compartment model differs from our coupled-ODE one in their considering known fluorophore-concentrations in the plasma compartment, (b) their non-modelling of fluorescence propagation that is significant in our settings, (c) the scaling factors of the PK parameters used in [17] cannot be obtained from measured boundary

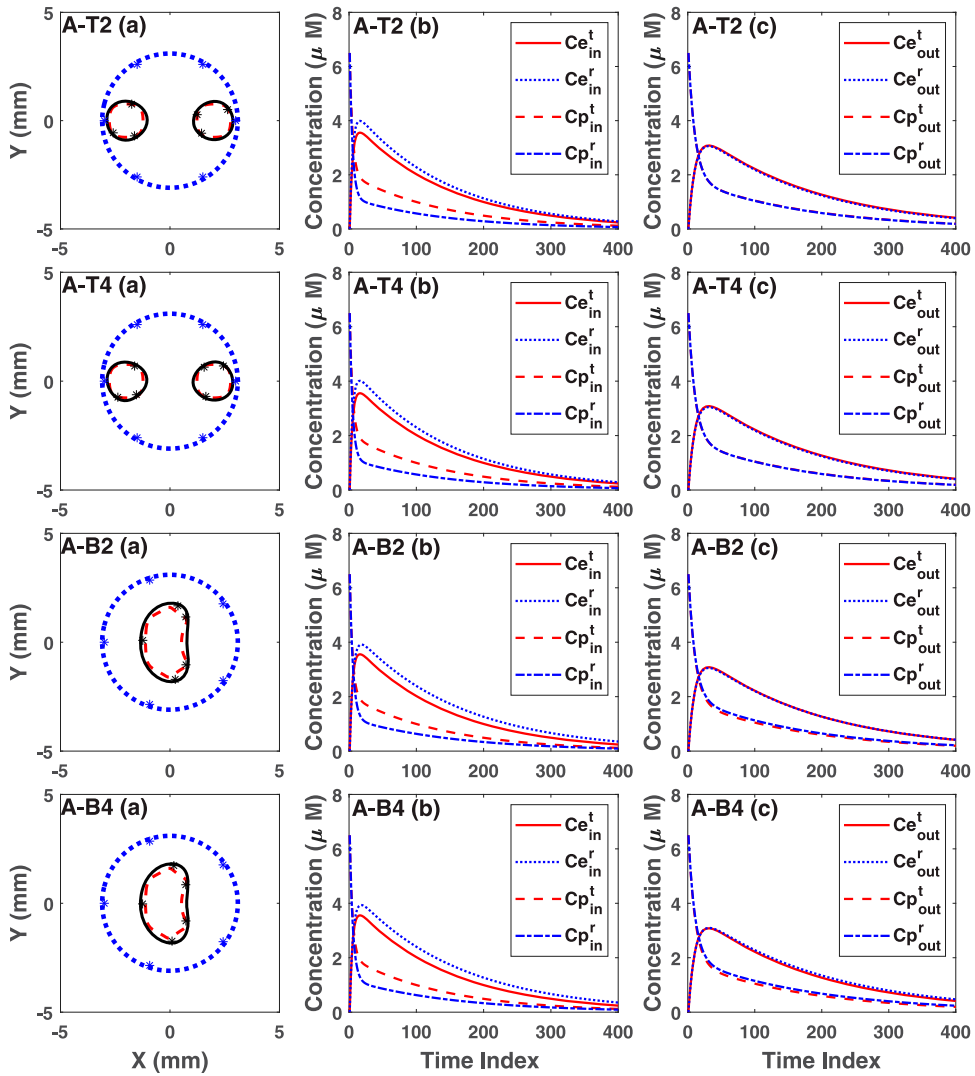


Figure 5. Jacobain-based reconstruction of two object and bean phantoms (labelled (a)), and concentration vs time plot (labelled (b), (c)) in AC tumour; (top-to-down: data-sets A-T2, A-T4, A-B2, A-B4) In the left column (a), blue dotted line denotes the initial level-set, red dashed line denotes the shape of true object, and solid black line denotes the reconstructed shape. In the 2nd and 3rd columns, red denotes the decay of concentration in true phantom (with superscript t) and blue denotes the decay in reconstructed phantom (with superscript r). The 2nd column shows C_e and C_p plots inside the tumour region. The 3rd column shows C_e and C_p plots outside the tumour region. 1 time-index = 5 seconds.

pressure data, and, (d) their needing a temporally constant fluence in various compartments in their formulation, assuming the fluence only changing in pixels where the contrast agent accumulates with the endogeneous fluence staying constant.

The NMSE for k_{pe} range from -38.7 to -27.19 dB in gradient filter compared with -44.3 to -35.8 dB in GN-filter across all SNRs. The NMSE for k_{ep} range from -31.9 to -18.54 in gradient filter compared with -30 to -21.8 dB in GN-filter. Alacam et al.

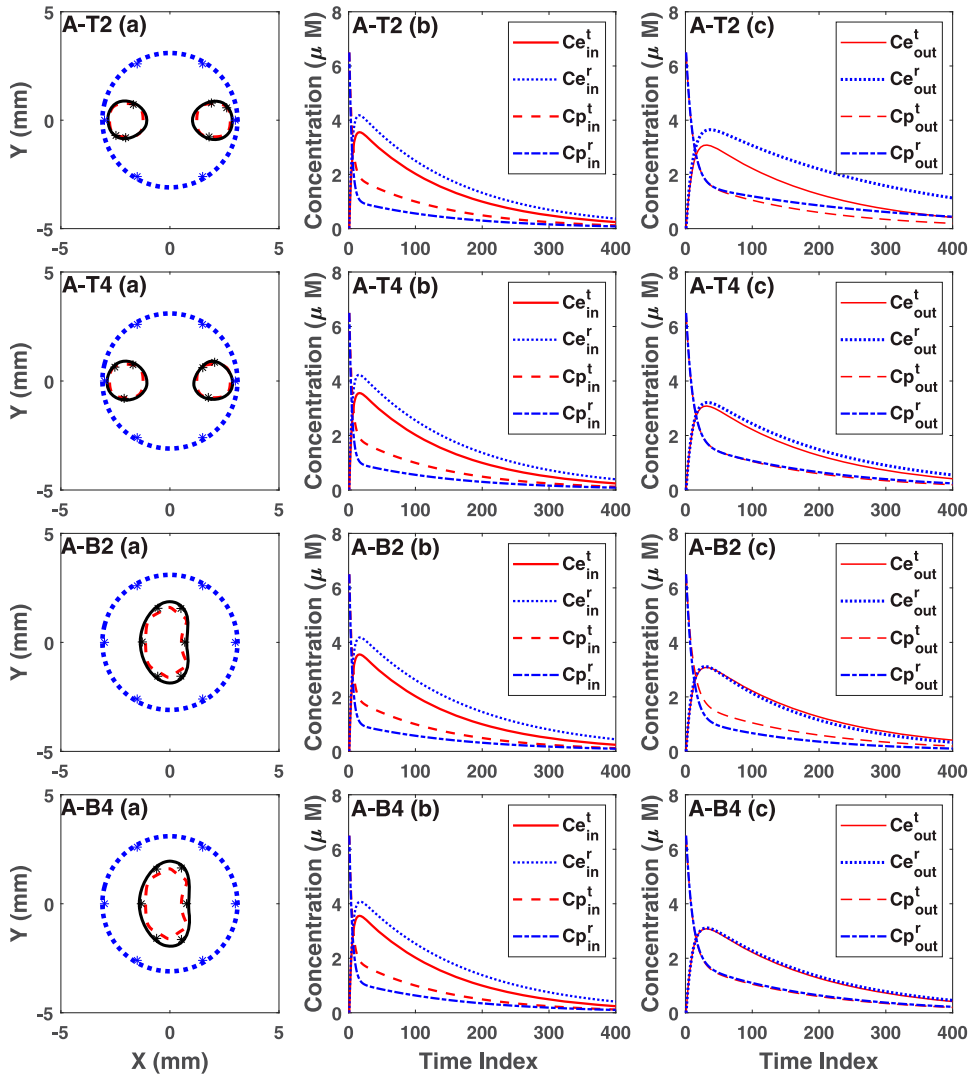


Figure 6. Gradient-based reconstruction of two object and bean phantoms (labelled (a)), and concentration vs time plot (labelled (b), (c)) in AC tumour; (top-to-down: data-sets A-T2, A-T4, A-B2, A-B4) In the left column (a), blue dotted line denotes the initial level-set, red dashed line denotes the shape of true object, and solid black line denotes the reconstructed shape. In the 2nd and 3rd columns, red denotes the decay of concentration in true phantom (with superscript t) and blue denotes the decay in reconstructed phantom (with superscript r). The 2nd column shows C_e and C_p plots inside the tumour region. The 3rd column shows C_e and C_p plots outside the tumour region. 1 time-index = 5 seconds.

[9] reconstructs pointwise estimates of pharmacokinetic rates using fluorescence optical tomography (FOT) in a Kalman filter framework. Alacam et al. [9] reports NMSEs of -19.77 and -18.49 dB for k_{pe} and k_{ep} , respectively, using noiseless data in a synthetic phantom. In our previous work on fluorescence-based pharmacokinetics [11], for the same phantoms considered in this work, we reported NMSEs in the range of -31 to -16.9 dB for k_{pe} and -31.3 to -20.9 dB for k_{ep} . We have observed an improvement in the reconstructed

Table 6. Error measures for the reconstructions using GN-filter (for the two object case the centroid error is an ordered pair (a,b) corresponding to each object).

Phantom	$E_{AP}\%$	E_C (mm)	$D(U, V)$	$E_{NMSE}(k)$
I-T1	0.54	(0.0078, 0.0052)	0.9196	0.109
I-T2	0.54	(0.0078, 0.0040)	0.9201	0.109
I-T3	0.61	(0.0116, 0.0041)	0.9095	0.107
I-T4	0.60	(0.0121, 0.0040)	0.9114	0.106
I-B1	0.76	0.0546	0.6436	0.099
I-B2	0.76	0.0546	0.6436	0.100
I-B3	0.76	0.0563	0.6436	0.099
I-B4	0.76	0.0501	0.6414	0.102
A-T1	0.49	(0.0171, 0.0084)	0.9109	0.044
A-T2	0.45	(0.0210, 0.0074)	0.9167	0.044
A-T3	0.42	(0.0195, 0.0141)	0.9226	0.045
A-T4	0.37	(0.0228, 0.0189)	0.9288	0.047
A-B1	0.80	0.0663	0.6150	0.045
A-B2	0.80	0.0663	0.6150	0.044
A-B3	0.80	0.0663	0.6150	0.044
A-B4	0.80	0.0673	0.6140	0.043

Table 7. Error measures for the reconstructions using gradient filter (for the two object case the centroid error is an ordered pair (a,b) corresponding to each object).

Phantom	$E_{AP}\%$	E_C (mm)	$D(U, V)$	$E_{NMSE}(k)$
I-T1	0.26	(0.0084, 0.0028)	0.9495	0.076
I-T2	0.45	(0.0128, 0.0136)	0.9182	0.065
I-T3	0.40	(0.0090, 0.0117)	0.9251	0.066
I-T4	0.36	(0.0167, 0.0146)	0.9330	0.071
I-B1	0.78	0.0503	0.6417	0.101
I-B2	0.77	0.0595	0.6505	0.082
I-B3	0.78	0.0588	0.6433	0.077
I-B4	0.78	0.0515	0.6427	0.077
A-T1	0.25	(0.0122, 0.0116)	0.9484	0.081
A-T2	0.37	(0.0246, 0.0253)	0.9284	0.076
A-T3	0.43	(0.0110, 0.0193)	0.9206	0.074
A-T4	0.37	(0.0143, 0.0124)	0.9256	0.086
A-B1	0.80	0.0766	0.6160	0.048
A-B2	0.80	0.0713	0.6206	0.063
A-B3	0.79	0.0683	0.6328	0.049
A-B4	0.80	0.0541	0.6635	0.041

values of volume fractions, v_e and v_p compared to our work in [11]. The NMSEs obtained here in gradient filter are in the range of -58.83 to -40.86 dB for v_e and -125.4 to -86.8 dB for v_p , whereas the NMSEs in [11] are ranging from -38.5 to -9.3 dB for v_e and -86.1 to -51 dB for v_p .

In addition, we observe the variation in the NMSEs between differing data-noise levels to be significantly lesser in our PK-FPAT results than in the earlier PK-FOT results of [11].

Thus, with respect to PK-FOT results reported in literature, our PK-FPAT results yield better reconstructions reflected in reduced values of reconstructed NMSEs across data-noise levels as well as more stable reconstructions as seen by lesser variation in the NMSEs between differing data-noise levels. Also, our computational experience showed a better stability of the iterates (lack of divergence) after reaching convergence with the PK-FPAT iterates than what we had seen with the PK-FOT reconstructions in [11].

Table 8. Values of $20 \log (\text{NMSE})$ dB for the spatial pharmacokinetic parameter and volume fraction values from GN-filter.

Phantom	$E(k_{pe})$ dB	$E(k_{ep})$ dB	$E(v_e)$ dB	$E(v_p)$ dB	$E(k_{elm})$ dB
I-T1	-35.85	-23.78	-55.71	-107.95	-36.36
I-T2	-36.15	-23.69	-55.93	-108.26	-36.02
I-T3	-36.84	-23.74	-56.25	-108.82	-36.26
I-T4	-37.35	-23.54	-56.37	-108.05	-33.36
I-B1	-37.18	-22.09	-42.41	-87.60	-31.34
I-B2	-37.31	-21.92	-42.43	-87.68	-31.12
I-B3	-36.11	-21.82	-42.44	-87.94	-30.10
I-B4	-38.44	-22.24	-42.29	-87.38	-34.09
A-T1	-44.35	-29.93	-64.30	-132.49	-32.49
A-T2	-43.55	-29.92	-63.07	-130.66	-32.49
A-T3	-42.65	-29.83	-61.62	-128.21	-32.39
A-T4	-40.99	-29.79	-59.63	-123.95	-32.51
A-B1	-38.82	-29.34	-42.05	-110.35	-33.33
A-B2	-38.56	-29.78	-42.03	-110.34	-33.04
A-B3	-38.17	-30.01	-42.01	-110.46	-32.26
A-B4	-37.52	-30.25	-42.05	-110.45	-30.69

Table 9. Values of $20 \log (\text{NMSE})$ dB for the spatial pharmacokinetic parameter and volume fraction values from gradient filter.

Phantom	$E(k_{pe})$ dB	$E(k_{ep})$ dB	$E(v_e)$ dB	$E(v_p)$ dB	$E(k_{elm})$ dB
I-T1	-36.49	-23.69	-57.37	-106.93	-30.42
I-T2	-38.70	-18.54	-56.70	-99.02	-17.90
I-T3	-37.45	-23.36	-58.62	-108.53	-21.82
I-T4	-37.372	-27.68	-54.54	-101.45	-35.99
I-B1	-27.19	-17.98	-40.86	-86.87	-31.94
I-B2	-35.10	-21.67	-42.54	-88.23	-23.76
I-B3	-33.89	-26.23	-42.27	-88.67	-34.49
I-B4	-35.72	-25.33	-42.55	-88.42	-33.94
A-T1	-33.89	-28.03	-57.57	-125.44	-29.67
A-T2	-33.48	-24.89	-57.98	-124.61	-18.40
A-T3	-33.94	-30.47	-58.83	-123.31	-33.22
A-T4	-33.44	-27.91	-56.43	-117.60	-30.83
A-B1	-33.94	-28.62	-42.70	-112.59	-30.65
A-B2	-28.73	-22.11	-41.83	-112.58	-12.11
A-B3	-36.82	-24.34	-42.96	-111.63	-25.49
A-B4	-30.73	-31.90	-42.30	-111.59	-32.79

To draw an explanation for the improved results, we recall that it has been mentioned [24,61], that FPAT/QPAT reconstruction schemes are stabler than their corresponding FOT/DOT counterparts due to the presence of intermediate absorbed optical energy density information, acting as the source of information in the entire domain.

In PK-FOT, we reconstruct the PK-parameters from the boundary fluence, where as in PK-FPAT, the PK parameter reconstruction involves implicitly recovering the absorbed optical energy density as an intermediate variable from the boundary pressure data, which improves the conditioning of the sensitivity matrices in PK-FPAT (compared to PK-FOT) and aids in the superior reconstructions and stability in PK parameters. In our work, we have observed that the log-plot of singular values for the PK-FOT Jacobians at the true-resolution corresponding to test cases have a steeper rate of decay and a larger number of very small singular values in our previous work [11], as compared to the present PK-FPAT

test cases which have a much flatter log-singular-value spectrum and very few really small singular values.

In summary, for the test cases considered, we observe that the reconstructions using the GF are as good as those from the GNF, and, PK-FPAT has improved the overall stability and quality of reconstructions as compared to PK-FOT.

Our work demonstrates the validation of fluorescence photoacoustic pharmacokinetic tomographic reconstruction framework on numerical testcases assuming ideal detection settings such as point detector and flat (unit) detector response in the frequency band. However, spatial and electrical impulse responses (corresponding to finite detector size/shape and frequency response, respectively) of a detector [62] can be simply incorporated into the photoacoustic forward model using convolution (in time domain) or multiplication (in frequency domain) [63]. In addition, laser repetition rates also need to be ensured to be rapid enough for the dynamic problem's instrumentation. The frequency band employed in our study is similar to those employed by the group of Dr. Huabei Jiang. In [55,64,65], they utilized 50 frequencies between 50 to 540 kHz to perform QPAT reconstructions. In [66,67], multispectral QPAT was demonstrated using the transducers with 1 MHz central frequency (0.65–1.18 MHz bandwidth). The circular transducer grid (radius: 1.5 cm) employed in [67] consisted of 120 detectors with the detector separation of 0.8 mm, which is similar to what we considered in our testcases. The data acquisition cards corresponding to such frequencies have been mentioned in literature such as in [68,69] and can be employed for experimental realization of the proposed tomographic modality.

7. Summary and conclusions

Pharmacokinetic rates of contrast agents provide quantitative physiological information for analysing the vascular permeability characteristics of blood vessels in the tissue, in early cancer detection and drug metabolism studies. Non-ionizing alternatives to nuclear medicine and radiological imaging modalities such as DCE-PET/MRI/CT, include DCE-MSOT, and the optical fluorescence-based FOT and FPAT.

The present work introduces for the first time in literature, a fully-nonlinear reconstruction framework for PK parameters and fluorophore-concentrations using the recent modality of fluorescence photoacoustic tomography (FPAT). We model the tomographic process by an optical-fluorescence modelled frequency domain photoacoustic equation along with a 2-compartment model for the pharmacokinetics.

We further introduce a trust region-based gradient-filter approach to solving the dynamic PK-FPAT reconstruction problem. We present both, Jacobian-based Gauss–Newton filter and gradient-based GF reconstruction schemes to retrieve the shape, optical and pharmacokinetic parameters of abnormalities directly from boundary pressure measurements. In a coupled-compartment modelled framework, we solve the dynamic FPAT state (compartment-concentration) and parameter (PK) estimation problem in a shape-based RBF level-set reconstruction scheme. The reconstruction algorithms are validated with numerical test studies on synthetic cancer mimicking phantoms. The much lower computation complexity for calculating the gradients as compared to the Jacobians [27,28] makes the GF the computationally less heavy (and more feasible) method for practical implementations compared to the GNF.

The use of the FPAT-based schemes for PK-tomography leads to more stable and superior reconstructions than those obtained by PK-FOT for similar test cases, while, with respect to current DCE-MSOT schemes, incorporating more complete forward models including optical fluorescence and coupled-ODE compartment models with no simplifying assumptions (within the accuracy of the models considered) on the fluence, and reconstructing actual (rather than scaled) PK-parameters, in a fully-nonlinear model-based reconstruction framework. With respect to PK-FOT results reported in literature, our PK-FPAT results yield better reconstructions reflected in reduced values of reconstructed normalized mean square error (NMSE) across data-noise levels as well as more stable reconstructions as seen by lesser variation in the NMSEs between differing data-noise levels. Also, our computational experience showed a better stability of the iterates (lack of divergence) after reaching convergence with the PK-FPAT iterates than what we had seen with our earlier reported PK-FOT reconstructions.

The detailed benchmarking studies carried out in the present work pave the way for application to system level studies including specific source-detector geometries, detector sensitivities, bandwidth and resolution issues, which are the subject of ongoing work.

In summary, we observe that for the test cases considered, the reconstructions using the GF are as good as those from the GNF, and, PK-FPAT has improved the overall stability and quality of reconstructions as compared to PK-FOT. The PK-tomographic reconstructions obtained demonstrate the capability of the proposed method to differentiate pathological conditions and quantify the changes in vascular permeability around the cancerous tissue thus establishing its potential as a non-ionizing alternative for PK-imaging.

Acknowledgments

The authors acknowledge the use of HPC Facility at IIT Kanpur. NN thanks Nishigandha Patil (PhD student, IIT-Kanpur) for useful presentation inputs.

Disclosure statement

No potential conflict of interest was reported by the author(s).

References

- [1] Bisdas S, Baghi M, Smolarz A, et al. Quantitative measurements of perfusion and permeability of oropharyngeal and oral cavity cancer, recurrent disease, and associated lymph nodes using first-pass contrast-enhanced computed tomography studies. *Invest Radiol*. 2007;42:172–179. DOI: 10.1097/01.rli.0000252496.74242.0b.
- [2] Cárdenas-Rodríguez J, Howison CM, Pagel MD. A linear algorithm of the reference region model for dce-mri is robust and relaxes requirements for temporal resolution. *Magn Reson Imaging*. 2013;31:497–507. DOI: 10.1016/j.mri.2012.10.008.
- [3] Klimas MT. Positron emission tomography and drug discovery: contributions to the understanding of pharmacokinetics, mechanism of action and disease state characterization. *Mol Imag Biol*. 2002;4:311–337. DOI: 10.1016/S1536-1632(02)00017-3.
- [4] Lammertsma AA, Hume SP. Simplified reference tissue model for pet receptor studies. *Neuroimage*. 1996;4:153–158. DOI: 10.1006/nimg.1996.0066.
- [5] Murase K. Efficient method for calculating kinetic parameters using t1-weighted dynamic contrast-enhanced magnetic resonance imaging. *Mag Reson Med: An Official J Int Soc Magn Reson Med*. 2004;51:858–862. DOI: 10.1002/mrm.20022.

- [6] O'Connor J, Tofts P, Miles K, et al. Dynamic contrast-enhanced imaging techniques: Ct and mri. *Br J Radiol.* **2011**;84:S112–S120. DOI: 10.1259/bjr/55166688.
- [7] Tofts PS, Brix G, Buckley DL, et al. Estimating kinetic parameters from dynamic contrast-enhanced T1-weighted MRI of a diffusable tracer: standardized quantities and symbols. *J Magn Reson Imaging.* **1999**;10:223–232. DOI: 10.1002/(SICI)1522-2586(199909)10:3<223::AID-JMRI2>3.0.CO;2-S.
- [8] Vigiante BL, Abraham SA, Michelich CR, et al. In vivo monitoring of tissue pharmacokinetics of liposome/drug using mri: illustration of targeted delivery. *Magn Reson Med: An Official J Int Soc Mag Reson Med.* **2004**;51:1153–1162. DOI: 10.1002/mrm.20074.
- [9] Alacam B, Yazici B. Direct reconstruction of pharmacokinetic-rate images of optical fluorophores from NIR measurements. *IEEE Trans Med Imaging.* **2009**;28:1337–1353. DOI: 10.1109/TMI.2009.2015294.
- [10] Alacam B, Yazici B, Intes X, et al. Pharmacokinetic-rate images of indocyanine green for breast tumors using near-infrared optical methods. *Phys Med Biol.* **2008**;53:837–859. DOI: 10.1088/0031-9155/53/4/002.
- [11] Gottam O, Naik N, Gambhir S. Parameterized level-set based pharmacokinetic fluorescence optical tomography using the regularized Gauss–Newton filter. *J Biomed Opt.* **2018**;24:031010. DOI: 10.1117/1.JBO.24.3.031010.
- [12] Gurfinkel M, Thompson AB, Ralston W, et al. Pharmacokinetics of ICG and HPPH-car for the detection of normal and tumor tissue using fluorescence, near-infrared reflectance imaging: a case study. *Photochem Photobiol.* **2000**;72:94–102. DOI: 10.1562/0031-8655(2000)0720094POIAHC2.0.CO2.
- [13] Wang X, Wu L, Yi X, et al. Performance enhancement of pharmacokinetic diffuse fluorescence tomography by use of adaptive extended Kalman filtering. *Comput Math Methods Med.* **2015**; 2015. Article ID 739459. 15 pp. DOI:10.1155/2015/739459.
- [14] Zhang G, Liu F, Zhang B, et al. Imaging of pharmacokinetic rates of indocyanine green in mouse liver with a hybrid fluorescence molecular tomography/x-ray computed tomography system. *J Biomed Opt.* **2013**;18:040505. DOI: 10.1117/1.JBO.18.4.040505.
- [15] Zhang G, Liu F, Pu H, et al. A direct method with structural priors for imaging pharmacokinetic parameters in dynamic fluorescence molecular tomography. *IEEE Trans Biomed Eng.* **2014**;61:986–990. DOI: 10.1109/TBME.2013.2292714.
- [16] Zhang G, Pu H, He W, et al. Full-direct method for imaging pharmacokinetic parameters in dynamic fluorescence molecular tomography. *Appl Phys Lett.* **2015**;106:081110. DOI: 10.1063/1.4913690.
- [17] Hupple CW, Morscher S, Burton NC, et al. A light-fluence-independent method for the quantitative analysis of dynamic contrast-enhanced multispectral optoacoustic tomography (dce msot). *Photoacoustics.* **2018**;10:54–64. DOI: 10.1016/j.pacs.2018.04.003.
- [18] Morscher S, Driessen WH, Claussen J, et al. Semi-quantitative multispectral optoacoustic tomography (msot) for volumetric pk imaging of gastric emptying. *Photoacoustics.* **2014**;2:103–110. DOI: 10.1016/j.pacs.2014.06.001.
- [19] Song W, Tang Z, Zhang D, et al. Comprehensive studies of pharmacokinetics and biodistribution of indocyanine green and liposomal indocyanine green by multispectral optoacoustic tomography. *RSC Adv.* **2015**;5:3807–3813. DOI: 10.1039/C4RA09735A.
- [20] Taruttis A, Morscher S, Burton NC, et al. Fast multispectral optoacoustic tomography (msot) for dynamic imaging of pharmacokinetics and biodistribution in multiple organs. *PLoS ONE.* **2012**;7:e30491. DOI: 10.1371/journal.pone.0030491.
- [21] Xiao TG, Weis JA, Gayzik FS, et al. Applying dynamic contrast enhanced msot imaging to intratumoral pharmacokinetic modeling. *Photoacoustics.* **2018**;11:28–35. DOI: 10.1016/j.pacs.2018.07.003.
- [22] Gottam O, Naik N, Pandey PK. RBF level-set based fluorescence photoacoustic pharmacokinetic tomography. *Computational Optical Sensing and Imaging.* 2020. p. JF4E–7. DOI: 10.1364/COSI.2020.JF4E.7.
- [23] Pandey PK, Gottam O, Naik N, et al. Comparative study of one-step and two-step quantitative fluorescence photoacoustic tomography. *Appl Opt.* **2019**;58:3116–3127. DOI: 10.1364/AO.58.003116.

- [24] Ren K, Zhao H. Quantitative fluorescence photoacoustic tomography. *SIAM J Imaging Sci.* **2013**;6:2404–2429. DOI: 10.1137/130912323.
- [25] Razansky D, Distel M, Vinegoni C, et al. Multispectral opto-acoustic tomography of deep-seated fluorescent proteins in vivo. *Nat Photonics.* **2009**;3:412–417. DOI: 10.1038/nphoton.2009.98.
- [26] Yang D, Wang H, Sun C, et al. Development of a high quantum yield dye for tumour imaging. *Chem Sci.* **2017**;8:6322–6326. DOI: 10.1039/C7SC02698F.
- [27] Pandey PK, Gottam O, Naik N, et al. Gradient-based one-step fluorescence photoacoustic tomography. *Appl Opt.* **2020**;59:4357–4366. DOI: 10.1364/AO.382879.
- [28] Pandey PK, Bharadwaj J, Naik N, et al. One-step fluorescence photoacoustic tomography with the optical radiative transfer model. *JOSA A.* **2020**;37:1175–1192. DOI: 10.1364/JOSAA.389476.
- [29] Ren K, Zhang R, Zhong Y. Inverse transport problems in quantitative pat for molecular imaging. *Inverse Probl.* **2015**;31:125012. DOI: 10.1088/0266-5611/31/12/125012.
- [30] Aghasi A, Kilmer M, Miller EL. Parametric level set methods for inverse problems. *SIAM J Imaging Sci.* **2011**;4:618–650. DOI: 10.1137/100800208.
- [31] Naik N, Beatson R, Eriksson J. Radial-basis-function level-set-based regularized Gauss–Newton-filter reconstruction scheme for dynamic shape tomography. *Appl Opt.* **2014**;53:6872–6884. DOI: 10.1364/AO.53.006872.
- [32] Naik N, Beatson R, Eriksson J, et al. An implicit radial basis function based reconstruction approach to electromagnetic shape tomography. *Inverse Probl.* **2008**;25:025004. DOI: 10.1088/0266-5611/25/2/025004.
- [33] Zacharopoulos AD, Arridge SR, Dorn O, et al. Three-dimensional reconstruction of shape and piecewise constant region values for optical tomography using spherical harmonic parametrization and a boundary element method. *Inverse Probl.* **2006**;22:1509–1532. DOI: 10.1088/0266-5611/22/5/001.
- [34] Morrison N. Tracking filter engineering: the Gauss–Newton and polynomial filters. London: The Institution of Engineering and Technology; **2013**.
- [35] Cuccia DJ, Bevilacqua F, Durkin AJ, et al. In vivo quantification of optical contrast agent dynamics in rat tumors by use of diffuse optical spectroscopy with magnetic resonance imaging coregistration. *Appl Opt.* **2003**;42:2940–2950. DOI: 10.1364/AO.42.002940.
- [36] Yuan Z, Jiang H. Quantitative photoacoustic tomography: recovery of optical absorption coefficient maps of heterogeneous media. *Appl Phys Lett.* **2006**;88:231101. DOI: 10.1063/1.2209883.
- [37] Bagchi S, Roy D, Vasu RM. Forward problem solution in photoacoustic tomography by discontinuous Galerkin method. *Bio-Optics: design and application*; 2011. p. JTua22. DOI: 10.1364/BODA.2011.JTuA22.
- [38] Gan H, Levin P, Ludwig R. Finite element formulation of acoustic scattering phenomena with absorbing boundary condition in the frequency domain. *J Acoust Soc Am.* **1993**;94:1651–1662. DOI: 10.1121/1.408138.
- [39] Fedele F, Laible J, Eppstein M. Coupled complex adjoint sensitivities for frequency-domain fluorescence tomography: theory and vectorized implementation. *J Comput Phys.* **2003**;187:597–619. DOI: 10.1016/S0021-9991(03)00150-5.
- [40] Milstein AB, Webb KJ, Bouman CA. Estimation of kinetic model parameters in fluorescence optical diffusion tomography. *JOSA A.* **2005**;22:1357–1368.
- [41] Eppstein MJ, Fedele F, Laible J, et al. A comparison of exact and approximate adjoint sensitivities in fluorescence tomography. *IEEE Trans Med Imaging.* **2003**;22:1215–1223. DOI: 10.1109/TMI.2003.818165.
- [42] Reynolds JS, Thompson CA, Webb KJ, et al. Frequency domain modeling of reradiation in highly scattering media. *Appl Opt.* **1997**;36:2252–2259.
- [43] Alacam B, Yazici B, Intes X, et al. Extended Kalman filtering for the modeling and analysis of ICG pharmacokinetics in cancerous tumors using NIR optical methods. *IEEE Trans Biomed Eng.* **2006**;53:1861–1871. DOI: 10.1109/TBME.2006.881796.
- [44] Chen CT. Linear system theory and design. New York: Oxford University Press, Inc.; **1999**.

- [45] Su MY, Mühler A, Lao X, et al. Tumor characterization with dynamic contrast-enhanced MRI using mr contrast agents of various molecular weights. *Magn Reson Med.* **1998**;39:259–269. DOI: 10.1002/mrm.1910390213.
- [46] Chan TF, Vese LA. Active contours without edges. *IEEE Trans Image Process.* **2001**;10:266–277. DOI: 10.1109/83.902291.
- [47] Naik N, Patil N, Yadav Y, et al. Fully nonlinear SP_3 approximation based fluorescence optical tomography. *IEEE Trans Med Imaging.* **2017**;36:2308–2318. DOI: 10.1109/TMI.2017.2718028.
- [48] Naik N, Eriksson J, de Groen P, et al. A nonlinear iterative reconstruction and analysis approach to shape-based approximate electromagnetic tomography. *IEEE Trans Geosci Remote Sens.* **2008**;46:1558–1574. DOI: 10.1109/TGRS.2008.916077.
- [49] Schweiger M, Arridge SR, Nissilä I. Gauss–Newton method for image reconstruction in diffuse optical tomography. *Phys Med Biol.* **2005**;50:2365. DOI: 10.1088/0031-9155/50/10/013.
- [50] Nocedal J, Wright S. Numerical optimization, series in operations research and financial engineering. New York USA: Springer; **2006**.
- [51] de Sturler E, Kilmer ME. A regularized Gauss–Newton trust region approach to imaging in diffuse optical tomography. *SIAM J Sci Comput.* **2011**;33:3057–3086. DOI: 10.1137/100798181.
- [52] Conn AR, Gould NI, Toint PL Trust region methods. Vol. 1, Philadelphia: SIAM; **2000**. DOI: 10.1137/1.9780898719857.
- [53] Pulkkinen A, Cox BT, Arridge SR, et al. Direct estimation of optical parameters from photoacoustic time series in quantitative photoacoustic tomography. *IEEE Trans Med Imaging.* **2016**;35:2497–2508. DOI: 10.1109/TMI.2016.2581211.
- [54] Saratoon T, Tärvinen T, Cox B, et al. A gradient-based method for quantitative photoacoustic tomography using the radiative transfer equation. *Inverse Probl.* **2013**;29:075006.
- [55] Yuan Z, Jiang H. A calibration-free, one-step method for quantitative photoacoustic tomography. *Med Phys.* **2012**;39:6895–6899.
- [56] Wang LV, Wu Hi.. Biomedical optics: principles and imaging. New Jersey: John Wiley & Sons; **2012**.
- [57] Treeby BE, Cox BT. k-wave: Matlab toolbox for the simulation and reconstruction of photoacoustic wave fields. *J Biomed Opt.* **2010**;15:021314. DOI: 10.1117/1.3360308.
- [58] Oppenheim AV. Discrete-time signal processing. New Delhi: Pearson Education India; **1999**.
- [59] Wang K, Su R, Oraevsky AA, et al. Investigation of iterative image reconstruction in three-dimensional optoacoustic tomography. *Phys Med Biol.* **2012**;57:5399–5423. DOI: 10.1088/0031-9155/57/17/5399.
- [60] Wang X, Zhang Y, Zhang L, et al. Direct reconstruction in CT-analogous pharmacokinetic diffuse fluorescence tomography: two-dimensional simulative and experimental validations. *J Biomed Opt.* **2016**;21:046007–046007. DOI: 10.1117/1.JBO.21.4.046007.
- [61] Kuchment P, Steinhauer D. Stabilizing inverse problems by internal data. *Inverse Probl.* **2012**;28:084007.
- [62] Caballero MAA, Rosenthal A, Buehler A, et al. Optoacoustic determination of spatio-temporal responses of ultrasound sensors. *IEEE Trans Ultrason Ferroelectr Freq Control.* **2013**;60:1234–1244.
- [63] Rosenthal A, Ntziachristos V, Razansky D. Model-based optoacoustic inversion with arbitrary-shape detectors. *Med Phys.* **2011**;38:4285–4295.
- [64] Yuan Z, Wang Q, Jiang H. Reconstruction of optical absorption coefficient maps of heterogeneous media by photoacoustic tomography coupled with diffusion equation based regularized newton method. *Opt Express.* **2007**;15:18076–18081.
- [65] Yuan Z, Zhang Q, Jiang H. Simultaneous reconstruction of acoustic and optical properties of heterogeneous media by quantitative photoacoustic tomography. *Opt Express.* **2006**;14:6749–6754.
- [66] Liu Y, Jiang H, Yuan Z. Two schemes for quantitative photoacoustic tomography based on monte carlo simulation. *Med Phys.* **2016**;43:3987–3997.
- [67] Liu Y, Yuan Z. Multi-spectral photoacoustic elasticity tomography. *Biomed Opt Express.* **2016**;7:3323–3334.

- [68] Sun Y, Sobel ES, Jiang H. First assessment of three-dimensional quantitative photoacoustic tomography for in vivo detection of osteoarthritis in the finger joints. *Med Phys.* **2011**;38:4009–4017.
- [69] Xiang L, Han B, Carpenter C, et al. X-ray acoustic computed tomography with pulsed x-ray beam from a medical linear accelerator. *Med Phys.* **2013**;40:010701.
- [70] Larusson F, Fantini S, Miller EL. Parametric level set reconstruction methods for hyperspectral diffuse optical tomography. *Biomed Opt Express.* **2012**;3:1006–1024. DOI: 10.1364/BOE.3.001006.

Appendices

Appendix 1

In this appendix, we summarize the requisite expressions corresponding to adjoint variables with respect to the coupled diffusion equation model for optical fluorescence propagation, that we require to evaluate the gradients in the GF. Using finite element discretization, the adjoint system of equations are given by [39] for the adjoint matrices Ψ_{xx} , Ψ_{xm} and Ψ_{mm} (these matrices are columnwise-stacked adjoint fields corresponding to each column of the RHS source-matrix), as:

$$\mathbf{A}_x \Psi_{xx} = \Delta_N; \quad \mathbf{A}_m \Psi_{mm} = \Delta_N; \quad \mathbf{A}_x \Psi_{xm} = \mathbf{M}_\beta \Psi_{mm} \quad (\text{A1})$$

where Δ_N is the identity matrix, \mathbf{A}_x , \mathbf{A}_m and \mathbf{M}_β are the assembled matrices of A_x , A_m and M_β , respectively, for all elements [39], with $A_x = \mathcal{A}(D_x, k_x, b_x)$, $A_m = \mathcal{A}(D_m, k_m, b_m)$, $M_\beta = \mathcal{M}(\beta)$, with

$$\mathcal{A}(D, k, b) = K_D + K_k + K_b; \quad \mathcal{M}(\beta) = K_\beta \beta. \quad (\text{A2})$$

where

$$\begin{aligned} K_D &= \left[\sum_{j=1}^3 \int_{\Omega_e} N_j^t D_j (\nabla[\mathbf{N}])^T \nabla[\mathbf{N}] \right], \\ K_k &= \left[\sum_{j=1}^3 \int_{\Omega_e} N_j^t k_j [\mathbf{N}]^T [\mathbf{N}] \right], \\ K_b &= \left[\sum_{j=1}^2 \int_{\partial\Omega_e} N_j^t b_j [\mathbf{N}]^T [\mathbf{N}] \right] \end{aligned}$$

Here N_j^t represents the linear basis functions for the triangular elements and $[\mathbf{N}] = [N_1^t \quad N_2^t \quad N_3^t]$.

Using finite element discretization, denoting by \mathbf{A} as the assembled matrix corresponding to \mathcal{A} , the sensitivity of the excitation and emission fluences with respect to nodal values μ_{axf}^i for $i = 1 \dots N$, are given by

$$\frac{\partial \Phi_x}{\partial \mu_{axf}^i} = -\Psi_{xx}^T \mathbf{A} \left(\frac{\partial D_x}{\partial \mu_{axf}^i}, \frac{\partial k_x}{\partial \mu_{axf}^i}, \frac{\partial b_x}{\partial \mu_{axf}^i} \right) \Phi_x \equiv -\Psi_{xx}^T \mathbf{A}_x^{\mu,i} \Phi_x \quad (\text{A3})$$

$$\begin{aligned} \frac{\partial \Phi_m}{\partial \mu_{axf}^i} &= -\Psi_{xm}^T \mathbf{A} \left(\frac{\partial D_x}{\partial \mu_{axf}^i}, \frac{\partial k_x}{\partial \mu_{axf}^i}, \frac{\partial b_x}{\partial \mu_{axf}^i} \right) \Phi_x - \Psi_{mm}^T \mathbf{A} \left(\frac{\partial D_m}{\partial \mu_{axf}^i}, \frac{\partial k_m}{\partial \mu_{axf}^i}, \frac{\partial b_m}{\partial \mu_{axf}^i} \right) \Phi_m \\ &\quad + \Psi_{mm}^T \mathbf{M} \left(\frac{\partial \beta}{\partial \mu_{axf}^i} \right) \Phi_x \\ &\equiv -\Psi_{xm}^T \mathbf{A}_x^{\mu,i} \Phi_x - \Psi_{mm}^T \mathbf{A}_m^{\mu,i} \Phi_m + \Psi_{mm}^T \mathbf{M}_\beta^{\mu,i} \Phi_x \end{aligned} \quad (\text{A4})$$

Appendix 2

The area-parameter product error measure[11,31,47], defined across all the measurement time instants is given by:

$$E_{AP} = \left(\left[\frac{\sum_{j=1}^M |\mu_{rec}^i(j)A_{rec} - \mu_{ac}^i(j)A_{ac}|}{\sum_{j=1}^M |\mu_{ac}^i(j)A_{ac}|} \right] / M \right) \times 100\%; \quad (A5)$$

where A_{ac} , A_{rec} represents the area of actual and reconstructed object, respectively, $\mu_{rec}^i(j)$ (respectively, $\mu_{ac}^i(j)$) represents reconstructed (respectively, actual) fluorophore absorption coefficient (14) inside tumor region at time instant j . Area of an object is given by

$$A_{object} = a_{element} \sum_{i,j} \chi_{object}(x_i, y_j) \quad (A6)$$

where $a_{element}$ is the area of an element (a constant in our studies), $\chi_{object}(\cdot)$ is the characteristic function with respect to object support, (i, j) represents the indices of centroid coordinates x and y of the discretized domain.

The centroid coordinates of an object are given by

$$\bar{x}_{object} = \frac{\sum_{i,j} x_i \chi_{object}(x_i, y_j)}{A_{object}}; \quad \bar{y}_{object} = \frac{\sum_{i,j} y_j \chi_{object}(x_i, y_j)}{A_{object}} \quad (A7)$$

The Euclidean distance between the centroids of reconstructed object and actual object is a useful error metric [11,31,47], and is given as:

$$E_c = \sqrt{(\bar{x}_{rec} - \bar{x}_{ac})^2 + (\bar{y}_{rec} - \bar{y}_{ac})^2} \quad (A8)$$

The Dice coefficient [70] quantifies the localization and similarity of the shape reconstruction with the original shape. If U denotes the set of nodes inside the reconstructed object and V denotes the set of nodes inside the true object, the Dice coefficient is given by

$$D(U, V) = \frac{2|U \cap V|}{|U| + |V|} \quad (A9)$$

$|U \cap V|$ denotes the number of nodes present in U and also belongs to V . The Dice coefficient varies from 0 (indicating complete mismatch) to 1 (indicating accurate shape reconstruction).

Appendix 3

PK:Pharmacokinetic, FOT:Fluorescence optical tomography, DCE-dynamic contrast enhancement, MSOT:Multispectral optoacoustic tomography, PET:Positron emission tomography, CT:Computerized tomography, MRI: Magnetic resonance imaging, FPAT: Fluorescence photoacoustic tomography, GNF: Gauss-Newton filter, GF:Gradient filter, RBF: Radial basis function, ODE: Ordinary differential equation, IV:intravenous, IDC: Invasive ductal carcinoma, AC: Adeno carcinoma, EES: Extracellular extravascular space, GN: Gauss-Newton, BFGS:Broyden-Fletcher-Goldfarb-Shanno, SNR: Signal-to-noise ratio, NMSE:Normalized mean square error